CHAPTER ONE

Ingredients

1.1 INTRODUCTION

Diode lasers, like most other lasers, incorporate an optical gain medium in a resonant optical cavity. The design of both the gain medium and the resonant cavity are critical in modern lasers. A sample schematic of a laser cavity and its elements is shown in Fig. 1.1. In this case, an optional mode selection filter is also added to permit only one cavity mode to lase. The gain medium consists of a material that normally absorbs incident radiation over some wavelength range of interest. But, if it is *pumped* by inputting either electrical or optical energy, the electrons within the material can be excited to higher, nonequilibrium energy levels, so the incident radiation can be amplified rather than absorbed by stimulating the de-excitation of these electrons along with the generation of additional radiation. The resonant optical cavity supports a number of cavity standing waves, or modes. As illustrated in Figs. 1.1b and c, these occur where the cavity length is a multiple of a half wavelength. If the resulting gain is sufficient to overcome the losses of some resonant optical mode of the cavity, this mode is said to have reached *threshold*, and relatively coherent light will be emitted. The resonant cavity provides the necessary positive feedback for the radiation being amplified, so that a lasing oscillation can be established and sustained above threshold pumping levels. A typical diode laser light-pump current characteristic is shown in Fig. 1.1d. The *threshold* can be identified on an output light power vs. pump characteristic by a sharp knee, as illustrated in Fig. 1.1d.

For various applications, a single lasing mode inside a laser cavity is preferred. Different methods in cavity design can be used to favor the lasing of one mode

Diode Lasers and Photonic Integrated Circuits, Second Edition.
Larry A. Coldren, Scott W. Corzine, and Milan L. Mašanović.

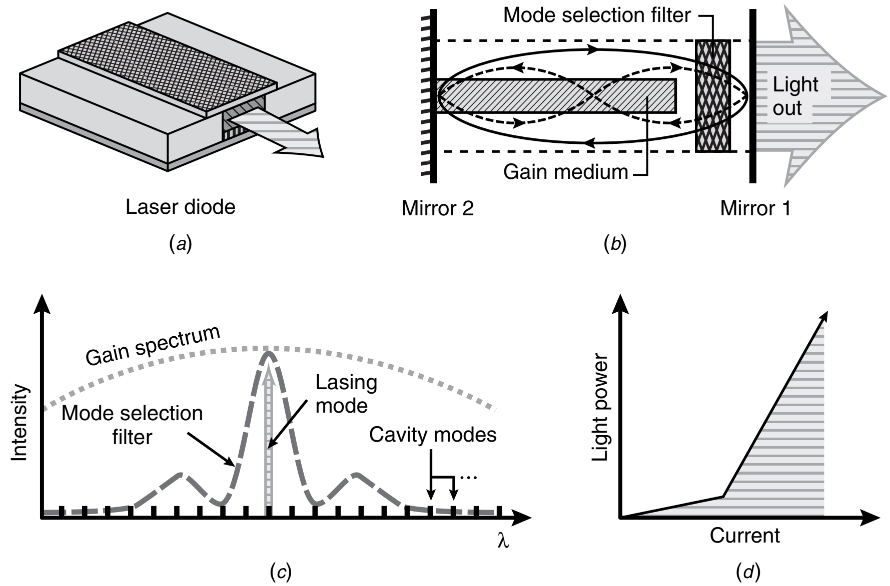

FIGURE 1.1: (a) A schematic of a simple laser diode. (b) Necessary ingredients for a single-frequency laser cavity—two mirrors, a gain medium, and a mode selection filter, which is required only for single wavelength λ operation. (c) Spectral characteristics of laser elements that get superimposed for single mode operation: cavity modes are given by $m \cdot \frac{\lambda}{2} = \bar{n}L$, where the mode number m is an integer, and $\bar{n}$ is the effective index of refraction (d) Typical light-current diode laser characteristic.

relative to others. The response of the optical mirrors can be tailored to support a single mode. Often, additional optical filtering elements will be incorporated inside the resonant cavity, to insure single mode operation of the laser. Fig. 1.1c shows the spectral response of the various elements of this cavity. This resonant optical cavity is defined by two broadband mirrors, with flat spectral responses, which define a number of cavity modes. An additional mode filtering element, with a defined bandpass optical transfer function, is included. The optical gain medium has a certain spectral response, which, in combination with the spectral response of the filter, will define which cavity mode will be singled out. As in any other oscillator, the output power level saturates at a level equal to the input minus any internal losses.

Since their discovery, lasers have been demonstrated in solid, liquid, gas and plasma materials. Today, the most important classes of lasers, besides the widespread *diode/(or semiconductor)* lasers are, *gas, dye, solid-state*, and *fiber* lasers, the latter really being fiber-optic versions of solid-state lasers. The helium–neon gas laser, the widely tunable flowing-dye laser, the Nd-doped YAG (yttrium–aluminum–garnet) solid-state and the Er or Yb-doped silica fiber lasers are four popular examples. Figure 1.2 shows commercial examples of Nd-YAG and dye lasers, an Er-doped fiber amplifier (EDFA), as well as a packaged diode

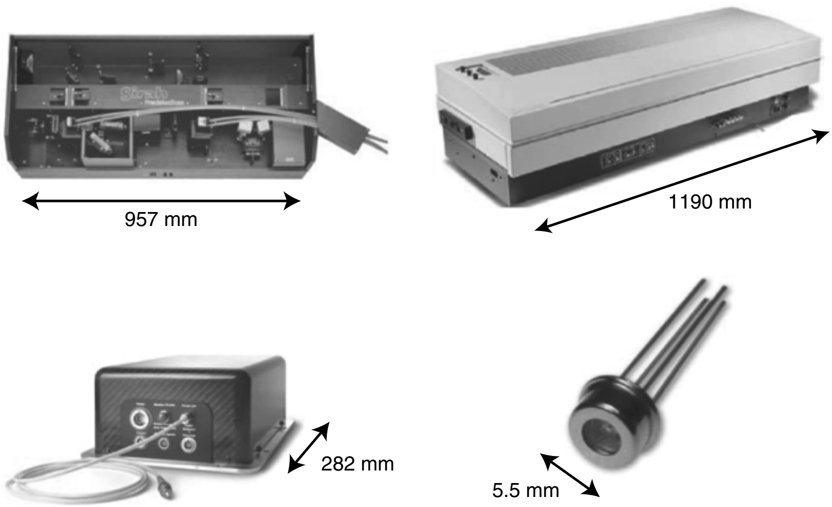

FIGURE 1.2: Examples of solid-state (upper left), dye (upper right), and fiber laser (bottom left) systems compared to a packaged diode laser chip (bottom right). To function, the diode laser also requires some drive electronics, and this increases its net size somewhat.

laser for comparison. The EDFA is used in fiber-optic systems to compensate losses, and with the addition of mirrors placed in the fiber, it can also become a laser. Diode lasers are distinguished from these other types primarily by their ability to be pumped directly by an electrical current. Generally, this results in a much more efficient operation. Overall power conversion efficiencies of $\sim$50% are not uncommon for a diode laser, whereas efficiencies on the order of 1% are common for gas and solid-state lasers, which traditionally have been pumped by plasma excitation or an incoherent optical flashlamp source, respectively. However, in recent years diode laser pumps have been used for both bulk solid-state lasers as well as fiber lasers, and wall plug efficiencies better than 25% have been achieved. Efficiencies of some gas lasers can be somewhat higher than that of the He-Ne laser, such as in the case of the CO_2 gas laser, which has a typical efficiency of over 10%. Another type of gas laser, the so-called Excimer laser, uses transitions between highly excited atomic states to produce high-power ultraviolet emission, and these are used in the medical industry for a variety of surgical procedures as well as in the semiconductor industry for patterning very fine features. Dye lasers are almost always used in a research environment because of their relatively high maintenance requirements, and they are generally pumped by other high power bench-top lasers. Their appeal is that their output wavelength can be tuned by as much as 10% for a given dye and mirror set, and by changing these, wavelengths from the near IR through much of the visible can be provided from a single commercial product.

Because of their longer cavities gas, dye, solid-state and fiber lasers also tend to have more coherent outputs than simple semiconductor lasers. However, more sophisticated single-frequency diode lasers can have comparable linewidths in the low megahertz range.

Another major attribute of diode lasers, their high reliability or useful lifetime, has led to their widespread use in important applications such as fiber-optic communications systems. Whereas the useful life of gas or flash-lamp-pumped solid-state lasers is typically measured in thousands of hours, that of carefully qualified diode lasers is measured in hundreds of years. Recent use of diode lasers to pump solid-state and fiber lasers may, however, provide the best advantages of both technologies, providing high reliability, improved efficiency, and low linewidth.

Net size is another striking difference between semiconductor and other lasers. Whereas gas, solid-state and fiber lasers are typically tens of centimeters in length, diode laser chips are generally about the size of a grain of salt, although the mounting and packaging hardware increases the useful component size to the order of a cubic centimeter or so. The diode lasers are mass-produced using wafer scale semiconductor processes, which makes them really inexpensive compared to all other types of lasers. The semiconductor origins of diode lasers allows for semiconductor integration techniques to be applied, and for multiple building blocks to be defined along the common waveguide, yielding functionally complex devices and opening a new field of photonic integrated circuits. Diode lasers with integrated optical amplifiers, modulators and similar other functions have been realized. In addition, monolithic widely tunable diode lasers and transmitters have been conceived and developed, in a footprint much smaller than that of external-cavity widely tunable lasers. Arrays of diode lasers and transmitters have been commercialized as well, for both optical pumping, and telecom purposes.

Diode lasers are used in many consumer products today. Examples are illustrated in Fig. 1.3. The most widely used diode lasers on the planet by far are those used in CD/DVD players, DVD ROM drives and optical mice. These diode lasers produce light beams in the red part of the visible spectrum at a wavelength of 0.65 μm. Recent improvements of the diode lasers emitting in the blue visible part of the spectrum have allowed for higher density DVD discs to be developed, resulting in the Blu-ray Disc technology, operating at 0.405 μm. Visible red diode lasers have replaced helium-neon lasers in supermarket checkout scanners and other bar code scanners. Laser printers are commonly used to produce high-resolution printouts, enabled by the high resolution determined by the wavelength of the diode laser used (780 nm or lower). Laser pointers, patient positioning devices in medicine utilize diode lasers emitting in the visible spectrum, both red and green.

In fiber-optic communication systems, diode lasers are primarily used as light sources in the optical links. For short reach links, a directly modulated diode laser is used as a transmitter. For longer reach links, diode lasers are used in conjunction with external modulators, which can be external to the diode laser chip, or integrated on the same chip. Complex diode laser-based photonic integrated circuits are currently deployed in a number of optical networks. In addition, Erbium doped fiber amplifiers, a key technology that is utilized for signal amplification in the existing fiber-optic networks, has in part been enabled by the development of high power, high reliability diode pump lasers.

FIGURE 1.3: Examples of the most common products that utilize diode lasers. (left) red laser in a DVD player shown in laptop computer; (center-top) blue laser in a Blu-ray Disc player; (center-bottom) red laser in a laser printer; (right-top) red laser in a bar-code scanner; (right-bottom) red (and sometimes green or blue) laser in a pointer.

There are many other areas where diode lasers are utilized. In medical applications, diode lasers are used in optical coherence tomography, an optical signal acquisition and processing method allowing extremely high quality, micrometer-resolution, three-dimensional images from within optical scattering media (e.g., biological tissue) to be obtained. In remote sensing, diode lasers are used in light detection and ranging (LIDAR) technology, new generation of optical radars that offer much improved resolution compared to the classical radio-frequency radars, due to light's much shorter wavelength. Other, similar applications are in range finding and military targeting.

In this chapter, we shall attempt to introduce some of the basic ingredients needed to understand semiconductor diode lasers. First, energy levels and bands in semiconductors are described starting from background given in Appendix 1. The interaction of light with these energy levels is next introduced. Then, the enhancement of this interaction by carrier and photon confinement using heterostructures is discussed. Materials useful for diode lasers and how epitaxial layers of such materials can be grown is briefly reviewed. The lateral patterning of these layers to provide lateral current, carrier, and photon confinement for practical lasers is introduced. Finally, examples of different diode lasers are given at the end of the chapter.

1.2 ENERGY LEVELS AND BANDS IN SOLIDS

To begin to understand how gain is accomplished in lasers, we must have some knowledge of the energy levels that electrons can occupy in the gain medium. The allowed energy levels are obtained by solving Schrdinger's equation using the appropriate electronic potentials. Appendix 1 gives a brief review of this important solid-state physics, as well as the derivation of some other functions that we shall need later. Figure 1.4 schematically illustrates the energy levels that might be associated with optically induced transitions in both an isolated atom and a semiconductor solid. Electron potential is plotted vertically.

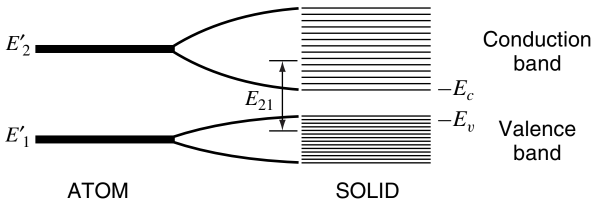

FIGURE 1.4: Illustration of how two discrete energy levels of an atom develop into bands of many levels in a crystal.

In gas and solid-state lasers, the energy levels of the active atomic species are only perturbed slightly by the surrounding gas or solid host atoms, and they remain effectively as sharp as the original levels in the isolated atom. For example, lasers operating at the 1.06 μm wavelength transition in Nd-doped YAG, use the $^4F_{3/2}$ level of the Nd atom for the upper laser state #2 and the $^4I_{11/2}$ level for the lower laser state #1. Because only these atomic levels are involved, emitted or absorbed photons need to have almost exactly the correct energy, $E_{21} = hc/1.06$ μm.

On the other hand, in a covalently bonded solid like the semiconductor materials we use to make diode lasers, the uppermost energy levels of individual constituent atoms each broaden into bands of levels as the bonds are formed to make the solid. This phenomenon is illustrated in Fig. 1.4. The reason for the splitting can be realized most easily by first considering a single covalent bond. When two atoms are in close proximity, the outer valence electron of one atom can arrange itself into a low-energy *bonding* (symmetric) charge distribution concentrated between the two nuclei, or into a high-energy *antibonding* (antisymmetric) distribution devoid of charge between the two nuclei. In other words, the isolated energy level of the electron is now split into two levels due to the two ways the electron can arrange itself around the two atoms.[1] In a covalent bond, the electrons of the two atoms both occupy the lower energy bonding level (provided they have opposite spin), whereas the higher energy antibonding level remains empty.

If another atom is brought in line with the first two, a new charge distribution becomes possible that is neither completely bonding nor antibonding. Hence, a third energy level is formed between the two extremes. When N atoms are covalently bonded into a linear chain, N energy levels distributed between the lowest-energy bonding state and the highest-energy antibonding state appear, forming a band of energies. In our linear chain of atoms, spin degeneracy allows all N electrons to fall into the lower half of the energy band, leaving the upper half of the band empty. However in a three-dimensional crystal, the number of energy levels is more generally equated with the number of *unit cells*, not the number of atoms. In

[1]The energy level splitting is often incorrectly attributed to the Pauli exclusion principle, which forbids electrons from occupying the same energy state (and thus forces the split, as the argument goes). In actuality, the splitting is a fundamental phenomenon associated with solutions to the wave equation involving two coupled systems and applies equally to probability, electromagnetic, or any other kind of waves. It has nothing to do with the Pauli exclusion principle.

typical semiconductor crystals, there are two atoms per primitive unit cell. Thus, the first atom fills the lower half of the energy band (as with the linear chain), whereas the second atom fills the upper half, such that the energy band is entirely full.

The semiconductor *valence* band is formed by the multiple splitting of the highest occupied atomic energy level of the constituent atoms. In semiconductors, the valence band is by definition entirely filled with no external excitation at $T = 0$ K. Likewise, the next higher-lying atomic level splits apart into the *conduction* band, which is entirely empty in semiconductors without any excitation. When thermal or other energy is added to the system, electrons in the valence band may be excited into the conduction band analogous to how electrons in isolated atoms can be excited to the next higher energy level of the atom. In the solid then, this excitation creates holes (missing electrons) in the valence band as well as electrons in the conduction band, and both can contribute to conduction.

Although Fig. 1.4 suggests that many conduction—valence band state pairs may interact with photons of energy E_{21}, Appendix 1 shows that the imposition of momentum conservation in addition to energy conservation limits the interaction to a fairly limited set of state pairs for a given transition energy. This situation is illustrated on the electron energy versus k-vector ($E - k$) plot shown schematically in Fig. 1.5. (Note that momentum $\equiv \hbar\mathbf{k}$.) Because the momentum of the interacting photon is negligibly small, transitions between the conduction and valence band must have the same k-vector, and only vertical transitions are allowed on this diagram. This fact will be very important in the calculation of gain.

1.3 SPONTANEOUS AND STIMULATED TRANSITIONS: THE CREATION OF LIGHT

With a qualitative knowledge of the energy levels that exist in semiconductors, we can proceed to consider the electronic transitions that can exist and the interactions

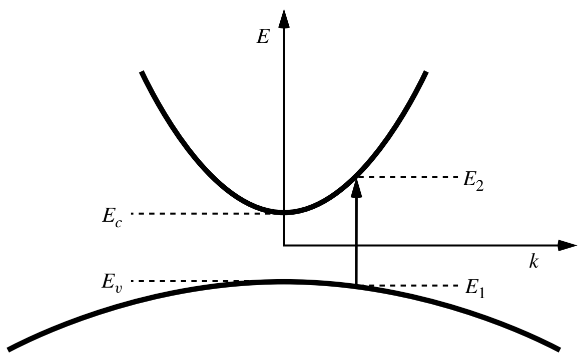

FIGURE 1.5: Electron energy vs. wave vector magnitude in a semiconductor showing a transition of an electron from a bound state in the valence band (E_1) to a free carrier state in the conduction band (E_2). The transition leaves a hole in the valence band. The lowest and highest energies in the conduction and valence bands are E_c and E_v, respectively.

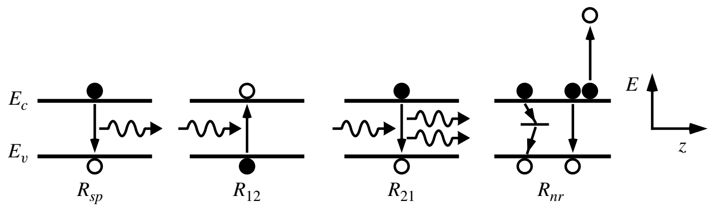

FIGURE 1.6: Electronic transitions between the conduction and valence bands. The first three represent radiative transitions in which the energy to free or bind an electron is supplied by or given to a photon. The fourth illustrates two nonradiative processes.

with lightwaves that are possible. Figure 1.6 illustrates the different kinds of electronic transitions that are important, emphasizing those that involve the absorption or emission of photons (lightwave quanta).

Although we are explicitly considering semiconductors, only a single level in both the conduction and valence bands is illustrated. As discussed earlier and in Appendix 1, momentum conservation selects only a limited number of such pairs of levels from these bands for a given transition energy. In fact, if it were not for a finite bandwidth of interaction owing to the finite state lifetime, a single pair of states would be entirely correct. In any event, the procedure to calculate gain and other effects will be to find the contribution from a single state pair and then integrate to include contributions from other pairs; thus, the consideration of only a single conduction–valence band state pair forms an entirely rigorous basis.

As illustrated, *four basic electronic recombination/generation (photon emission/absorption) mechanisms* must be considered separately:

1. Spontaneous recombination (photon emission)
2. Stimulated generation (photon absorption)
3. Stimulated recombination (coherent photon emission)
4. Nonradiative recombination

The open circles represent unfilled states (holes), and the solid circles represent filled states (electrons). Because electron and hole densities are highest near the bottom or top of the conduction or valence bands, respectively, most transitions of interest involve these carriers. Thus, photon energies tend to be only slightly larger than the bandgap (i.e., $E_{21} = h\nu \sim E_g$). The effects involving electrons in the conduction band are all enhanced by the addition of some pumping means to increase the electron density to above the equilibrium value there. Of course, the photon absorption can still take place even if some pumping has populated the conduction band somewhat.

The first case (R_{sp}) represents the case of an electron in the conduction band recombining spontaneously with a hole (missing electron) in the valence band to generate a photon. Obviously, if a large number of such events should occur, relatively incoherent emission would result because the emission time and direction would be random, and the photons would not tend to contribute to a coherent radiation field. This is the primary mechanism within a light-emitting diode (LED), in which photon feedback is not provided. Because spontaneous recombination requires the presence of an electron–hole pair, the recombination rate tends to be proportional to the product of the density of electrons and holes, NP. In undoped active regions, charge neutrality requires that the hole and electron densities be equal. Thus, the spontaneous recombination rate becomes proportional to N^2.

The second illustration (R_{12}) outlines photon absorption, which stimulates the generation of an electron in the conduction band while leaving a hole in the valence band.

The third process (R_{21}) is exactly the same as the second, only the sign of the interaction is reversed. Here an incident photon perturbs the system, stimulating the recombination of an electron and hole and simultaneously generating a new photon. *Of course, this is the all-important positive gain mechanism that is necessary for lasers to operate.* Actually, it should be realized that the net combination of stimulated emission and absorption of photons, $(R_{21} - R_{12})$, will represent the net gain experienced by an incident radiation field. In an undoped active region, net stimulated recombination (photon emission) depends on the existence of photons in addition to a certain value of electron density to overcome the photon absorption. Thus, as we shall later show more explicitly, the net rate of stimulated recombination is proportional to the photon density, N_p, multiplied by $(N - N_{tr})$, where N_{tr} is a *transparency* value of electron density (i.e., where $R_{21} = R_{12}$).

Finally, the fourth schematic in Fig. 1.6 represents the several nonradiative ways in which a conduction band electron can recombine with a valence band hole without generating any useful photons. Instead, the energy is dissipated as heat in the semiconductor crystal lattice. Thus, this schematic represents the ways in which conduction band electrons can escape from usefully contributing to the gain, and as such these effects are to be avoided if possible. In practice, there are two general nonradiative mechanisms for carriers that are important. The first involves nonradiative recombination centers, such as point defects, surfaces, and interfaces, in the active region of the laser. To be effective, these do not require the simultaneous existence of electrons and holes or other particles. Thus, the recombination rate via this path tends to be directly proportional to the carrier density, N. The second mechanism is Auger recombination, in which the electron–hole recombination energy, E_{21}, is given to another electron or hole in the form of kinetic energy. Thus, again for undoped active regions in which the electron and hole densities are equal, Auger recombination tends to be proportional to N^3 because we must simultaneously have the recombining electron–hole pair and the third particle that receives the ionization energy. Appendix 2 gives techniques for calculating the carrier density from the density of electronic states and the probability that they are occupied, generally characterized by a Fermi function.

1.4 TRANSVERSE CONFINEMENT OF CARRIERS AND PHOTONS IN DIODE LASERS: THE DOUBLE HETEROSTRUCTURE

As discussed in the previous section, optical gain in a semiconductor can only be achieved through the process of stimulated recombination (R_{21}). Therefore, a constant flow of carriers must be provided to replenish the carriers that are being recombined and converted into photons in the process of providing gain. For this flow of carriers in the gain material to happen, the semiconductor must be pumped or excited with some external energy source. A major attribute of diode lasers is their ability to be pumped directly with an electrical current. Of course, the active material can also be excited by the carriers generated from absorbed light, and this process is important in characterizing semiconductor material before electrical contacts are made. However, we shall focus mainly on the more technologically important direct current injection technique in most of our analysis.

The carrier-confining effect of the double–heterostructure (DH) is one of the most important features of modern diode lasers. After many early efforts that used homojunctions or single heterostructures, the advent of the DH structure made the diode laser truly practical for the first time and led to two Nobel prize awards in physics in the year 2000. Figure 1.7 gives a schematic of a broad-area *pin* DH laser diode, along with transverse sketches of the energy gap, index of refraction, and resulting optical mode profile across the DH region. As illustrated, a thin slab of undoped active material is sandwiched between p- and n-type cladding layers, which have a higher conduction–valence band energy gap. Typical thicknesses of the active layer for this simple three-layer structure are $\sim$0.1–0.2 μm. Because the bandgap of the cladding layers is larger, light generated in the active region will not have sufficient photon energy to be absorbed in them (i.e., $E_{21} = h\nu < E_{gcl}$).

For this DH structure, a transverse (x-direction) potential well is formed for electrons and holes that are being injected from the n- and p-type regions, respectively, under forward bias. As illustrated in part (b), they are captured and confined together, thereby increasing their probability of recombining with each other. In fact, unlike in most semiconductor diodes or transistors that are to be used in purely electronic circuits, it is desirable to have all the injected carriers recombine in the active region to form photons in a laser or LED. Thus, simple pn-junction theory, which assumes that all carriers entering the depletion region are swept through with negligible recombination, is totally inappropriate for diode lasers and LEDs. In fact, a better assumption for lasers and LEDs is that all carriers recombine in the i-region. Appendix 2 also discusses a possible "leakage current," which results from some of the carriers being thermionically emitted over the heterobarriers before they can recombine.

To form the necessary resonant cavity for optical feedback, simple cleaved facets can be used because the large index of refraction discontinuity at the semiconductor–air interface provides a reflection coefficient of $\sim$30%. The lower bandgap active region also usually has a higher index of refraction, n, than the cladding, as outlined in Fig. 1.7c, so that a transverse dielectric optical waveguide is formed with its axis along the z-direction. The resulting transverse optical energy density

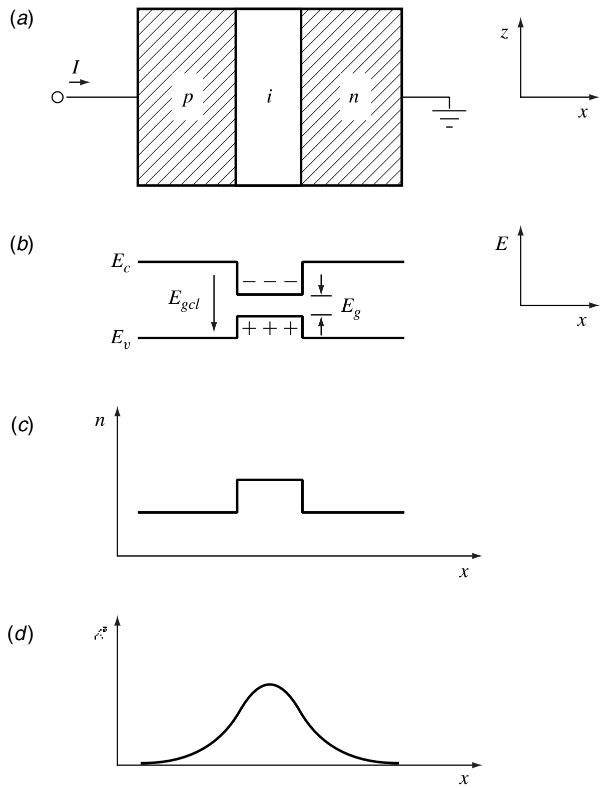

FIGURE 1.7: Aspects of the double-heterostructure diode laser: (a) a schematic of the material structure; (b) an energy diagram of the conduction and valence bands vs. transverse distance; (c) the refractive index profile; and (d) the electric field profile for a mode traveling in the z-direction.

profile (proportional to the photon density or the electric field magnitude squared, $|\mathscr{E}|^2$) is illustrated in Fig. 1.7d.

Thus, with the in-plane waveguide and perpendicular mirrors at the ends, a complete resonant cavity is formed. Output is provided at the facets, which only partially reflect. Later we shall consider more complex reflectors that can provide stronger feedback and wavelength filtering function, as illustrated in Fig 1.1. One should also realize that if the end facet reflections are suppressed by antireflection coatings, the device would then function as an LED. When we analyze lasers in the next chapter, the case of no feedback will also be considered.

The thickness of the active region in a DH plays an important role in its optical properties. If this thickness starts to get below ~100 nm, quantum effects on optical properties must be taken into account, and this regime of operation will be referred to as the *quantum confined* regime. For dimensions larger than 100 nm, we can assume that we are working with a continuum of states, and this regime is called the *bulk* regime.

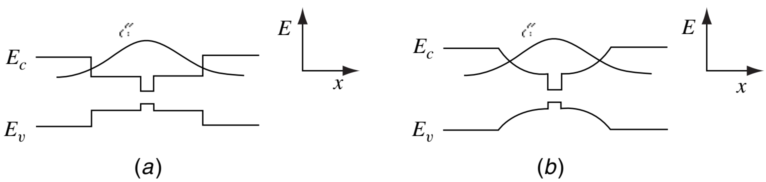

FIGURE 1.8: Transverse band structures for two different separate-confinement heterostructures (SCHs): (a) standard SCH; (b) graded-index SCH (GRINSCH). The electric field (photons) are confined by the outer step or graded heterostructure; the central quantum well confines the electrons.

It turns out that many modern diode lasers involve a little more complexity in their transverse carrier and photon confinement structure as compared to Fig. 1.7, but the fundamental concepts remain valid. For example, with in-plane lasers, where the light propagates parallel to the substrate surface, a common departure from Fig. 1.7 is to use a thinner *quantum-well* carrier-confining active region ($d \sim 10$ nm) and a surrounding intermediate bandgap *separate confinement* region to confine the photons. Figure 1.8 illustrates transverse bandgap profiles for such separate-confinement heterostructure, single quantum-well (SCH-SQW) lasers. The transverse optical energy density is also overlaid to show that the photons are confined primarily by the outer heterointerfaces and the carriers by the inner quantum well. Quantum-well active regions reduce diode laser threshold current and improve their efficiency and their thermal properties. The important concepts related to the quantum-well active regions are introduced in Appendix 1 and further discussed in detail in Chapter 4.

Example 1.1 An InP/InGaAsP double-heterostructure laser cross-section consists of a 320 nm tall InGaAsP separate confinement heterostructure waveguide region with the bandgap corresponding to 1.3 μm (1.3 Q), clad by InP on both sides.

Problem: (1) Determine the effective index of the fundamental transverse mode of this waveguide. (2) Determine the rate of decay of the normalized electric field U.

Solution: To solve this problem, we utilize the tools from the Appendix 3. Because this optical waveguide structure is symmetric, we can utilize the expression (A3.14) to solve for the effective index. Then, we can compute the wave vector component along x, k_x, and the decay constant γ using Equation (A3.7). From the problem statement, the refractive index of the InGaAsP region can be found in Table 1.1, $n_{\mathrm{II}} = 3.4$.
For the cladding, the refractive index value at 1.55 μm is $n_{\mathrm{I}} = n_{\mathrm{III}} = 3.17$. From Eq. (A3.12), the normalized frequency, V, is given by

$$V = k_0 d (n_{\mathrm{II}}^2 - n_{\mathrm{III}}^2)^{\frac{1}{2}} = \frac{2\pi}{1.55\ \mu\mathrm{m}}\ 0.32\ \mu\mathrm{m}\ (3.4^2 - 3.17^2)^{\frac{1}{2}} = 1.594$$

Using Eq. (A3.14), we can compute the value of the normalized propagation parameter b,

$$b = 1 - \frac{\ln\left(1 + \frac{V^2}{2}\right) \cdot}{\frac{V^2}{2}} = 1 - \frac{\ln\left(1 + \frac{1.594^2}{2}\right)}{\frac{1.594^2}{2}} = 0.354$$

and the effective index value,

$$\bar{n} = (n_{\rm II}^2 b + n_{\rm I}^2(1-b))^{\frac{1}{2}} = (3.4^2 \cdot 0.354 + 3.17^2 \cdot (1 - 0.354))^{\frac{1}{2}} = 3.253$$

To determine the minimum thickness of the top p doped cladding, we can compute the decay constant γ using Eq. (A3.7), remembering that the propagation constant $\beta = k_0 \bar{n}$,

$$\gamma = k_0(\bar{n}^2 - n_{\rm I}^2)^{\frac{1}{2}} = \frac{2\pi}{1.55\ \mu\text{m}}\ (3.253^2 - 3.17^2)^{\frac{1}{2}} = 2.9591\ \mu\text{m}^{-1}$$

Thus, for a 1 μm thick cladding, the optical energy decays to exp $(-2.9591) = 0.0027$ at the top surface. We can observe that the rate of decay is strongly dependent on the refractive index difference between the waveguide and the cladding—-for a larger difference, the field intensity outside the waveguide region decays faster. In a real laser, the active region would probably be defined by a set of quantum wells in the center of the InGaAsP double heterostructure region. This would complicate solving for the effective index, and this case will be treated in Chapter 6, when we talk about the perturbation theory.

1.5 SEMICONDUCTOR MATERIALS FOR DIODE LASERS

The successful fabrication of a diode laser relies very heavily on the properties of the materials involved. There is a very limited set of semiconductors that possess all the necessary properties to make a good laser. For the desired double heterostructures at least two compatible materials must be found, one for the cladding layers and another for the active region. In more complex geometries, such as the SCH mentioned earlier, three or four different bandgaps may be required within the same structure. The most fundamental requirement for these different materials is that they have the same crystal structure and nearly the same lattice constant, so that single-crystal, defect-free films of one can be *epitaxially* grown on the other. Defects generally become nonradiative recombination centers, which can steal many of the injected carriers that otherwise would provide gain and luminescence. In a later section we shall discuss some techniques for performing this epitaxial growth, but first we need to understand how to select materials that meet these fundamental boundary conditions.

Table 1.1 lists the lattice constants, bandgaps, effective masses, and indices of refraction for some common materials. (Subscripts on effective masses, C, HH,

TABLE 1.1: Material Parameters for III–V Compounds

III–V Compounds	a (Å)	E_g (eV) 0 K	E_g (eV) 300 K	m_C	m_{HH}	m_{LH}	m_{SH}	ε@dc	n@E_g	n@(λ μm)
GaAs	5.6533	1.519	1.424	0.067	0.38	0.09	0.15	13.2	3.62	3.52(0.98)
AlGaAs (0.2)	5.6548	1.769	1.673	0.084	0.39	0.1	0.16	12.5	3.64	3.46(0.87); 3.39(0.98)
AlAs*	5.660	2.228	2.153	0.19	0.48	0.2	0.29	10.06	3.2	2.98(0.87); 2.95(0.98)
InGaAs (0.2) comp. strained on GaAs	5.6533	1.296	1.215	0.059	0.37	0.062	0.11	13.6	3.6	
					0.078†	0.16†				
InP	5.8688	1.424	1.351	0.077	0.61	0.12	0.20	12.4	3.41	3.21(1.3); 3.17(1.55)
InGaAsP (1.3 μm)	5.8688	1.029	0.954	0.056	0.42	0.055	0.1	13.3	3.52	3.40(1.55)
InGaAsP (1.55 μm)	5.8688	0.874	0.800	0.045	0.37	0.044	0.08	13.75	3.55	
InGaAs (1.65 μm)	5.8688	0.818	0.748	0.046	0.36	0.041	0.07	13.9	3.56	
InAs	6.0583	0.418	0.359	0.027	0.34	0.027	0.05	15.15	3.52	
GaP*	5.4505	2.35	2.272	0.254	0.67	0.17	0.46	11.1	3.5	
AlP*	5.4635	2.505	2.41	0.21	0.51	0.21	0.3	9.8	2.97	
AlSb*	6.1355	1.696	1.63	0.33	0.47	0.16	0.24	12.0	3.5	
GaSb	6.0959	0.811	0.70	0.041	0.27	0.05	0.08	15.69	3.92	
InSb	6.4794	0.237	0.175	0.014	0.34	0.016	0.03	16.8	3.5	
GaN‡ (hexagonal)	$a = 3.189$	3.50	3.39	0.20 (‖)				8.9	2.67	2.52(0.41)
	$c = 5.185$			0.20 (⊥)						
AlN‡ (hexagonal)	$a = 3.112$	6.28	6.20	0.32 (‖)				8.5	2.5	2.18(0.14)
	$c = 4.982$			0.30 (⊥)						
InN‡ (hexagonal)	$a = 3.545$	0.78	-	0.07 (‖)				15.3	3.15	2.93(0.82); 3.12(0.66)
	$c = 5.703$			0.07 (⊥)						
$In_{0.12}Ga_{0.88}N$‡ (410 nm)										2.77(0.41)

*Indirect gap.
†In-plane masses.
‡For more details on hole mass parameters, see [5].

LH, and SH, denote values in the conduction, heavy-hole, light-hole, and split-off bands, respectively.)

Figure 1.9 plots the bandgap versus lattice constant for several families of III–V semiconductors. These III–V compounds (which consist of elements from columns III and V of the periodic table) have emerged as the materials of choice for lasers that emit in the 0.7–1.6 μm wavelength range. This range includes the important fiber-optic communication bands at 0.85, 1.31, and 1.55 μm, the pumping bands for fiber amplifiers at 1.48 and 0.98 μm, the window for pumping Nd-doped YAG at 0.81 μm, and the wavelength used for classic DVD disc players at 0.65 μm. Most of these materials have a *direct gap* in *E*–*k* space, which means that the minimum and maximum of the conduction and valence bands, respectively, fall at the same k-value, as illustrated in Fig. 1.5. This facilitates radiative transitions because momentum conservation is naturally satisfied by the annihilation of the equal and opposite momenta of the electron and hole. (The momentum of the photon is negligible.)

The lines on this diagram represent ternary compounds, which are alloys of the binaries labeled at their end-points. The dashed lines represent regions of indirect gap. The areas enclosed by lines between three or four binaries represent quaternaries, which obviously have enough degrees of freedom that the energy gap can

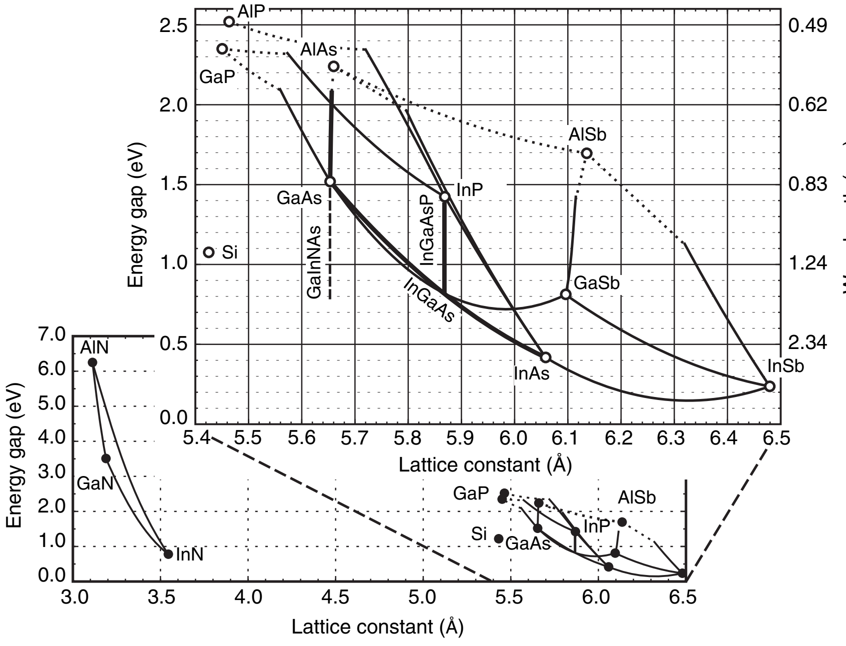

FIGURE 1.9: Energy gap vs. lattice constant of ternary compounds defined by curves that connect the illustrated binaries. The values in this plot were obtained from [2, 5] and are valid at $T = 0$ K. Details on how these values can be converted to room temperature values are given in the references cited.

be adjusted somewhat without changing the lattice constant. Thus, in general, a quaternary compound is required in a DH laser to allow the adjustment of the energy gap while maintaining lattice matching. Fortunately, there are some unique situations that allow the use of more simple ternaries. As can be seen, the AlGaAs ternary line is almost vertical. That is, the substitution of Al for Ga in GaAs does not change the lattice constant very much. Thus, if GaAs is used as the substrate, any alloy of $Al_xGa_{1-x}As$ can be grown, and it will naturally lattice match, so that no misfit dislocations or other defects should form. As suggested by the formula, the x-value determines the percentage of Al in the group III half of the III–V compound. The AlGaAs/GaAs system provides lasers in the 0.7–0.9 μm wavelength range. For DH structures in this system, about *two-thirds of the band offset* occurs in the conduction band. For shorter wavelengths into the red (e.g., 650 nm as used in DVDs), the AlInGaP/GaAs system is generally employed. In this case lattice matching requires a precise control of the ratios of Al:In:Ga in the quaternary regions.

The most popular system for long-distance fiber optics is the InGaAsP/InP system. Here the quaternary is specified by an x and y value (i.e., $In_{1-x}Ga_xAs_yP_{1-y}$). This is grown on InP to form layers of various energy gap corresponding to wavelengths in the 1.0–1.6 μm range, where silica fiber traditionally had minima in loss (1.55 μm) and dispersion (1.3 μm). Using InP as the substrate, a range of lattice-matched quaternaries extending from InP to the InGaAs ternary line can be accommodated, as indicated by the vertical line in Fig. 1.9. Fixing the quaternary lattice constant defines a relation between x and y. It has been found that choosing x equal to $\sim 0.47y$ results in approximate lattice matching to InP. The ternary endpoint is $In_{0.53}Ga_{0.47}As$. For DH structures in this system, only *about* 40% *of the band offset* occurs in the conduction band.

InGaAsP lasers and photonic integrated circuits (PICs) generally need to be operated at a constant temperature to maintain their performance. This is primarily due to the fact that with the increasing temperature, the electron leakage current from the quantum well increases. The main material parameter controlling the current leakage is the conduction band offset. Due to their much lighter effective mass, electrons require much tighter confinement with increasing temperature than holes. To improve the diode laser performance at high temperatures, particularly of interest for the fiber-optic metropolitan area network deployment, material engineering was successfully employed to increase the conduction band offset, through introduction of InGaAlAs material system. This material system enables quantum wells with the *conduction band offset of* $\Delta E_c = 0.7\Delta E_g$. Changing the barrier from $\Delta E_c = 0.4\Delta E_g$ to $\Delta E_c = 0.7\Delta E_g$ will lead to the reduction of the leakage current density from $J = 50$ A/cm^2 to $J = 1.5$ A/cm^2. Uncooled operation of lasers and integrated laser electroabsorption modulator PICs have been demonstrated at both 1310 nm and 1550 nm, and this remains an active area of research and deployment.

Lattice constants of ternary and quaternary compounds can be precisely calculated from Vegard's law, which gives a value equal to the weighted average of all the four possible constituent binaries. For example, in $In_{1-x}Ga_xAs_yP_{1-y}$, we obtain

$$a(x,y) = xya_{\mathrm{GaAs}} + x(1-y)a_{\mathrm{GaP}} + (1-x)ya_{\mathrm{InAs}} + (1-x)(1-y)a_{\mathrm{InP}}. \quad (1.1)$$

Similarly, the lattice constants for other alloys can be calculated. For example, in the AlInGaP/GaAs case, we would be considering a linear superposition of the lattice constants of the binaries AlP, InP, and GaP to match that of GaAs. And for InGaAlAs/InP, it would be the InAs, GaAs, AlAs binary lattice constants superimposed to match that of InP. The following example illustrates the application of the Vegard's law to the crystal lattice.

Example 1.2 InP-based 1550 nm vertical cavity surface emitting lasers have been made with AlAsSb/AlGaAsSb multilayer mirrors.

Problem: Calculate the fraction of As in the AlAsSb mirror layers for lattice matching to InP.

Solution: To solve this problem, we will use the Vegard's law. The composition of any AlAsSb alloy can be specified by value x, where x is the percentage of As in the alloy $\mathrm{AlSb}_{1-x}\mathrm{As}_x$. From Table 1.1, the lattice constants of InP, AlAs and AlSb are $a_{\mathrm{InP}} = 5.8688$ Å, $a_{\mathrm{AlAs}} = 5.660$ Å, and $a_{\mathrm{AlSb}} = 6.1355$ Å, respectively. Using Vegard's law,

$$a_{\mathrm{InP}} = xa_{\mathrm{AlAs}} + (1-x)a_{\mathrm{AlSb}}.$$

Therefore, the fraction of As in the lattice matched mirror layer is

$$x = \frac{a_{\mathrm{InP}} - a_{\mathrm{AlSb}}}{a_{\mathrm{AlAs}} - a_{\mathrm{AlSb}}} = 0.56.$$

Other parameters, for example, bandgap, can also be interpolated in a similar fashion to Eq. (1.1), however a second-order *bowing* parameter must oftentimes be added to improve the fit. The ternary lines in Fig. 1.9 were obtained using the following modified version of Vegard's law,

$$E_{gABC}(x) = xE_{gAB} + (1-x)E_{gAC} - x(1-x)C_{ABC}, \quad (1.2)$$

where C_{ABC} is an empirical bowing parameter.

When interpolating, one must be careful if different bands come into play in the process. For example, in AlGaAs, the values for GaAs and $\mathrm{Al}_{0.2}\mathrm{Ga}_{0.8}\mathrm{As}$ can be linearly extrapolated for direct gap AlGaAs up to $x \sim 0.45$, but at this point the indirect band minimum becomes the lowest, so the gap for higher x-values is then interpolated from this point using energy gap values that correspond to the first indirect band for both GaAs and AlAs. This extrapolation will be needed in some homework exercises. Here, we give a simple example of bandgap calculation in a ternary compound.

Example 1.3

Problem: A wurtzite structure GaInN quantum well contains 53% of Ga and 47% of N. The bowing parameter for the direct bandgap of this ternary is $C = 1.4$ eV. What is the bandgap of this quantum well?

Solution: To calculate the bandgap, we need to use Vegard's law, including the correction introduced by the bowing parameter. From Table 1.1, the direct bandgaps for GaN and InN are $E_{g1} = 3.510$ eV and $E_{g2} = 0.78$ eV, respectively. Using Eq. (1.2),

$$E_{gGaInN} = 0.53 \cdot E_{g1} + 0.47 \cdot E_{g2} - 0.53(0.47)1.4 \text{ eV} = 1.878 \text{ eV}.$$

In addition to the usual III–V compounds discussed earlier, Table 1.1 also lists some of the nitride compounds. These compounds had originally gained attention because of their successful use in demonstrating LEDs emitting at high energies in the visible spectrum. Whereas the InAlGaAsP based compounds are limited to emission in the red and near infrared regions, the nitrides have demonstrated blue and UV emission. GaN-based optoelectronic devices have achieved considerable progress since their first demonstration in 1996. Development of advanced epitaxial growth techniques, defect-reduced substrates, and sophisticated device design has resulted in high performance light-emitting diodes (LEDs) and laser diodes (LDs) with wide commercial presence. GaN-based LEDs have been particularly successful in solid-state lighting and display applications (traffic signal lights, automobile lights, flashlights), while laser diodes have emerged as critical components in the next generation of the high density DVD disk players (Blu-ray). Nitride components continue to generate considerable interest in such applications as projection displays, high resolution printing, and optical sensing, and thus remain an active area of research, development and commercialization.

Lattice matching is generally necessary to avoid defects that can destroy the proper operation of diode lasers. However, it is well known that a small lattice mismatch ($\Delta a/a \sim 1\%$) can be tolerated up to a certain thickness (~20 nm) without any defects. Thus, for a thin active region, one can move slightly left or right of the lattice matching condition illustrated in Fig. 1.9 or by Eq. (1.1). In this case, the lattice of the deposited film distorts to fit the substrate lattice in the plane, but it also must distort in the perpendicular direction to retain approximately the same unit cell volume it would have without distortion. Figure 1.10 shows a cross section of how unit cells might distort to accommodate a small lattice mismatch. After a critical thickness is exceeded, misfit defects are generated to relieve the integrated strain. However, up to this point, it turns out that such *strained layers* may have more desirable optoelectronic properties than their unstrained counterparts. In particular, due to their small dimensions of less than 10 nm, strained quantum wells can be created without introducing any undesired defects into the crystal. These structures will be analyzed in some detail in Chapter 4. In fact, it is fair to say that such strained-layer quantum wells, contained within separate-confinement

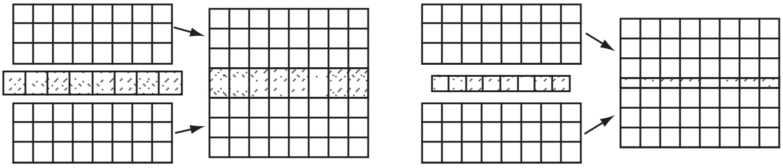

FIGURE 1.10: Schematic of sandwiching quantum wells with either a larger or smaller lattice constant to provide either compressive or tensile strain, respectively.

heterostructures as illustrated in Fig. 1.7, have become the most important form of active regions in modern diode lasers.

One of the key factors in determining the output wavelength of a quantum-well laser besides the material composition is the well width, or the so-called quantum-size effect. As illustrated in the following example, as a quantum-well is made more narrow, the lowest state energy is squeezed up from the well bottom, and the transition wavelength is made shorter. The barrier height plays an important role in this process as well because this limits the amount the energy can move away from the well bottom. These issues are covered in Appendix 1.

Example 1.4 An 80 Å wide quantum well composed of InGaAsP, lattice matched to InP, with the bandgap corresponding to 1.55 μm (1.55 Q), is surrounded by an InGaAsP barrier, lattice matched to InP, with the bandgap wavelength of 1.3 μm (1.3 Q).

Problem: Determine the energy and wavelength for photons generated in recombination between the ground states of the quantum well at room temperature.

Solution: In order to solve this problem, we utilize the tools from Appendix 1. We will determine the energy levels of this quantum well using Eq. (A1.14). First, we need to compute the energy of the ground state for this quantum well with infinitely high walls. Then, we need to determine the quantum numbers taking into account that this quantum well has finite walls, using Eq. (A1.17).

As mentioned in the problem statement, both the quantum well and the barrier are lattice matched to InP. From Table 1.1, $E_{\text{barrier}} = 0.954$ eV, and $E_{\text{well}} = 0.800$ eV. In this material system, only 40% of the band offset occurs in the conduction band. Therefore, the quantum well barrier height in the conduction band is given by $V_{0\text{C}} = 0.4\,(E_{\text{barrier}} - E_{\text{well}}) = 61.6$ meV and $V_{0\text{V}} = 0.6\,(E_{\text{barrier}} - E_{\text{well}}) = 92.4$ meV in the valence band.

From Eq. (A1.14), the ground state energy for a quantum well with infinite walls, $E_{1\text{c}}^{\infty}$, is given by

$$E_{1\text{c}}^{\infty} = 3.76\,\frac{m_0}{m}\left(\frac{100\ \text{Å}}{l}\right)^2\ \text{meV} = 3.76\,\frac{1}{0.045}\left(\frac{100}{80}\right)^2\ \text{meV} = 130.55\ \text{meV}$$

where $m = m_c$ was taken from Table 1.1. Similarly, for the valence band, $E_{1v}^{\infty} = 15.88$ meV, with $m = m_{HH}$. Now, we can calculate n_{max} for both quantum wells using Eq. (A1.17), $n_{maxc} = \sqrt{\frac{V_{0c}}{E_{1c}^{\infty}}} = 0.69$, and $n_{maxv} = \sqrt{\frac{V_{0v}}{E_{1v}^{\infty}}} = 2.41$. The normalized variable n_{max}, when rounded up to the nearest integer, yields the largest number of bound states possible. Either by reading the chart in Fig. A1.4 or using Eq. (A1.18), we can calculate the lowest quantum numbers for both cases:

$$n_{1c} \approx \frac{2}{\pi} \arctan\left[n_{maxc}\ (1 + 0.6^{n_{maxc}+1})\right] = 0.49$$

$$n_{1v} \approx \frac{2}{\pi} \arctan\left[n_{maxv}\ (1 + 0.6^{n_{maxv}+1})\right] = 0.78$$

Thus, $E_{1c} = n_{1c}^2 E_{1c}^{\infty} = 31.35$ meV and $E_{1v} = n_{1v}^2 E_{1v}^{\infty} = 9.66$ meV. Finally, the photon energy is given by

$$E_{photon} = E_{well} + E_{1c} + E_{1v} = 841.01 \text{ meV}.$$

This energy corresponds to the wavelength

$$\lambda = \frac{1.23985 \text{ eV } \mu\text{m}}{0.84101 \text{ eV}} = 1.47\ \mu\text{m}.$$

1.6 EPITAXIAL GROWTH TECHNOLOGY

To make the multilayer structures required for diode lasers, it is necessary to grow single-crystal lattice-matched layers with precisely controlled thicknesses over some suitable substrate. We have already discussed the issue of lattice matching and some of the materials involved. Here we briefly introduce several techniques to perform epitaxial growth of the desired thin layers.

We shall focus on the three most important techniques in use today: liquid-phase epitaxy (LPE), molecular beam epitaxy (MBE), and organometallic vapor-phase epitaxy (OMVPE). OMVPE is often also referred to as metal-organic chemical vapor deposition (MOCVD), although purists do not like the omission of the word *epitaxy*. As the names imply, the three techniques refer to growth either in liquid, vacuum, or a flowing gas, respectively. The growth under liquid or moderate pressure gas tends to be done near equilibrium conditions, so that the reaction can proceed in either the forward or reverse direction to add or remove material, whereas the MBE growth tends to be more of a physical deposition process. Thus, the near-equilibrium processes, LPE and MOCVD, tend to better provide for the removal of surface damage at the onset of growth, and they are known for providing higher quality interfaces generally important in devices. MBE on the other hand provides the ultimate in film uniformity and thickness control.

Figure 1.11 gives a cross section of a modern LPE system. In this system the substrate is placed in a recess in a graphite slider bar, which forms the bottom of

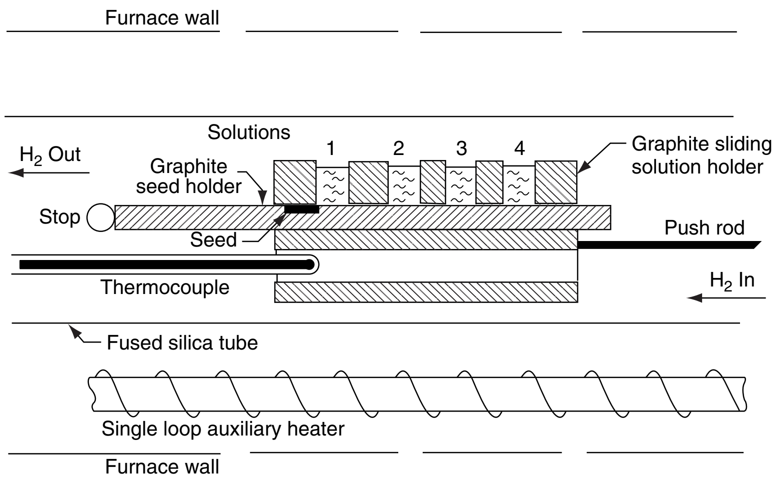

FIGURE 1.11: Schematic of a liquid-phase epitaxy (LPE) system [3]. (*Reprinted, by permission, from Applied Physics Letters*.)

a sequence of bins in a second graphite housing. The bins are filled with solutions from which a desired layer will grow as the substrate is slid beneath that bin. This entire assembly is positioned in a furnace, which is accurately controlled in temperature. There are several different techniques of controlling the temperature and the dwell time under each melt, but generally the solutions are successively brought to saturation by reducing the temperature very slowly as the substrate wafer is slid beneath alternate wells. In modern systems, the process of slider positioning and adjusting furnace temperature is done by computer control for reproducibility and efficiency. However, LPE is rapidly being replaced by MOCVD for the manufacture of most diode lasers.

The melts typically consist mostly of one of the group III metals with the other constituents dissolved in it. For InGaAsP growth, In metal constitutes most of the melt. For an $In_{0.53}Ga_{0.47}$ as film only about 2.5% of Ga and 6% As is added to the melt for growth at 650°C. For InP growth only about 0.8% of P is added. Needless to say, the dopants are added in much lesser amounts. Thus, LPE growth requires some very accurate scales for weighing out the constituents and an operator with a lot of patience.

Figure 1.12 shows a schematic of an MOCVD system. The substrate is positioned on a susceptor, which is heated typically by rf induction, or in some cases, by resistive heaters. The susceptor is placed into a reactor, which is designed to produce a laminar gas flow over the substrate surface. The gas carrier different growth species, and by precise control of the species concentration and flow rates, substrate temperature and pressure, highly precise growth is accomplished. Both low-pressure and atmospheric-pressure systems are being used. Whereas the atmospheric-pressure system uses the reactant gases more effectively, the layer uniformity and the time required to flush the reactor before beginning a new layer

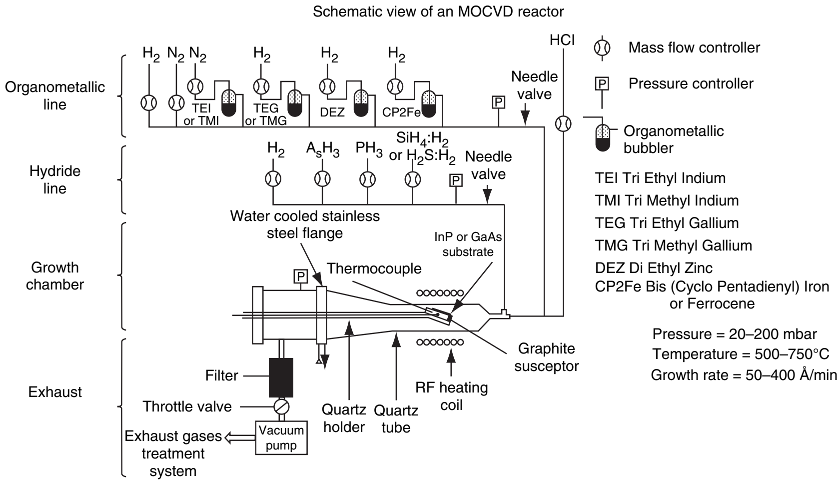

FIGURE 1.12: Schematic of a metal-organic chemical vapor deposition (MOCVD) system [1]. (*From GaInAsP Alloy Semiconductors, T. P. Pearsall, Ed., Copyright © John Wiley & Sons, Inc. Reprinted by permission of John Wiley & Sons, Inc.*)

is long. Low pressure is more popular where very abrupt interfaces between layers are desired, and this is very important for quantum-well structures. Typical growth temperature for InP based compounds is around 625°C.

As can be seen, a large part of the system is devoted to gas valving and manifolding to obtain the proper mixtures for insertion into the growth reactor chamber. The sources typically used for MOCVD consist of a combination of hydrides such as arsine (AsH_3), phosphine (PH_3), and organometallic liquids, which are used to saturate an H_2 carrier gas. Example organometallics are triethylindium and triethylgallium. Dopants can be derived from either other hydrides or liquid sources. For example, H_2S or triethyl-zinc can be used for n- or p-type dopants, respectively.

One of the key concerns with MOCVD is safety. The problems are primarily with the hydrides, which are very toxic. Thus, much of the cost of an MOCVD facility is associated with elaborate gas handling, monitoring, and emergency disposal techniques. Recently, there has been some industry effort to work with less toxic liquid sources for As and P (e.g., t-butyl-arsine and t-butyl-phosphine). Although still toxic, liquid sources give off only modest amounts of poisonous gases due to their vapor pressure, and such quantities could be accommodated by conventional fume hoods. Still, even though the hydrides have to be contained in high-pressure gas cylinders, which conceivably can fail and release large quantities of concentrated toxic gas in a short time, they remain the industry standard to this day.

Figure 1.14 shows a cross section of a solid-source MBE growth chamber. As illustrated, MBE is carried out under ultrahigh vacuum (UHV) conditions. Constituent beams of atoms are evaporated from effusion cells, and these condense on a heated substrate. Liquid nitrogen cryoshields line the inside of the system to

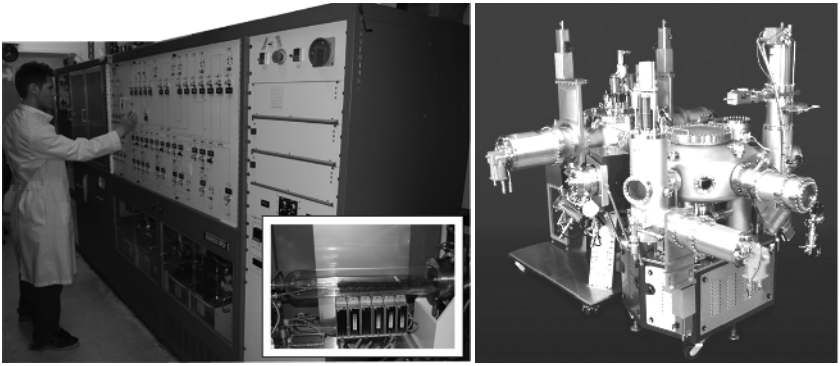

FIGURE 1.13: Photographs of (left) a single-wafer, horizontal flow MOCVD growth system at UC Santa Barbara, manufactured by Thomas Swan. The glass reactor, housing a graphite susceptor, is shown in the inset. Quartz heating lamps are visible underneath the reactor. (right) GEN20 MBE system, manufactured by Veeco, an ultra-flexible tool with a design configurable for III-V and emerging materials.

condense any stray gases. For stoichiometry control MBE makes use of the fact that the group V elements are much more volatile than the group III elements. Thus, if the substrate is sufficiently hot, the group V atoms will reevaporate unless there is a group III atom with which to form the compound. At the same time, the substrate must be sufficiently cool so that the group III atoms will stick. Therefore, the growth rate is determined by the group III flux, and the group V flux is typically set to several times that level. Typical growth temperatures for the AlGaAs system are in the 600–650°C range. However, because Al tends to oxidize easily, and such oxides create nonradiative recombination centers, AlGaAs lasers may be grown over 700°C.

One of the key features of MBE is that UHV surface analysis techniques can be applied to the substrate either before or during growth in the same chamber. One of the most useful tools is reflection high-energy electron diffraction (RHEED), which is an integral part of any viable MBE system. It is particularly useful in monitoring the growth rate *in situ* because the intensity of the RHEED pattern varies in intensity as successive monolayers are deposited.

Some hybrid forms of the last two techniques have also been developed (i.e., gas source MBE, metal-organic MBE (MOMBE), and chemical beam epitaxy (CBE) [7, 8]). These techniques are particularly interesting for the phosphorous-containing compounds, such as the important InGaAsP. Basically, gas-source MBE involves using the hydrides for the group V sources. Generally, these gases must be cracked by passing them through a hot cell prior to arriving at the substrate. MOMBE uses the metal-organics for the group III sources; again, some cracking is necessary. CBE is basically just ultralow-pressure MOCVD because both the group III and V sources are the same as in an MOCVD system. However, in the CBE case one still retains access to the UHV surface analysis techniques that have made MBE viable.

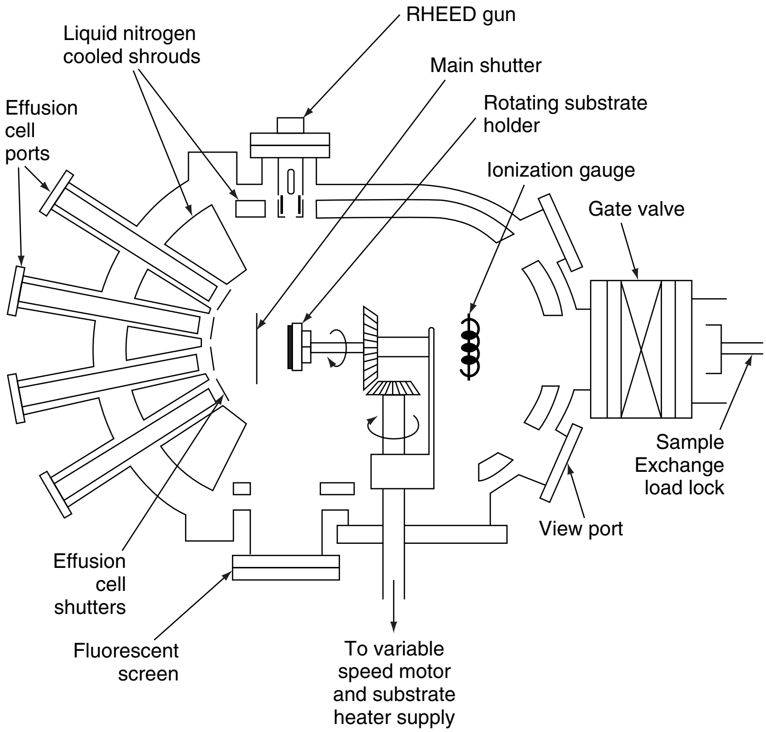

FIGURE 1.14: Schematic of a molecular beam epitaxy (MBE) system [4]. (*Reprinted, by permission, from Journal of Applied Physics.*)

Photographs of a research MOCVD and a research MBE system are shown in Fig. 1.13.

1.7 LATERAL CONFINEMENT OF CURRENT, CARRIERS, AND PHOTONS FOR PRACTICAL LASERS

Practical diode lasers come in two basic varieties: those with *in-plane* cavities and those with *vertical* cavities. The in-plane (or edge-emitting) types have been in existence since the late 1960s, whereas the vertical cavity (or vertical-cavity surface-emitting-laser–VCSEL for short) types have been viable only since about 1990. As mentioned earlier, feedback for the in-plane type can be accomplished with a simple cleaved-facet mirror; however, for vertical-cavity lasers a multilayer reflective stack must be grown below and above the active region for the necessary cavity mirrors. Figure 1.15 illustrates both types. Of course, many practical edge-emitters also use more complex mirrors as discussed in Chapter 3.

As suggested by this figure, practical lasers must emit light in a narrow beam, which implies that a *lateral* patterning of the active region is necessary. In the case

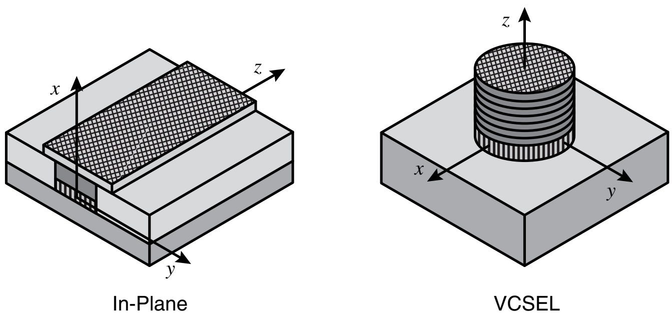

FIGURE 1.15: Schematic of in-plane and vertical-cavity surface-emitting lasers showing selected coordinate systems.

of the in-plane types, a stripe laser is formed that typically has lateral dimensions of a few microns. Similarly, the vertical-cavity types typically consist of a circular dot geometry with lateral dimensions of a few microns. This emitting aperture of a few microns facilitates coupling to optical fibers or other simple optics because it is sufficiently narrow to support only a single lateral mode of the resulting optical waveguide, but sufficiently wide to provide an emerging optical beam with a relatively small diffraction angle. However, in the case of the VCSEL there continues to be an important multimode-fiber optic market in which it is usually desired to use multimoded VCSELs that can fill the modal spectrum of the fibers.

Figure 1.16 shows cross-sectional scanning electron micrographs (SEMs) of both the in-plane and vertical-cavity lasers. The reference coordinate systems, also introduced in Fig. 1.15, are somewhat different for these two generic types of diode lasers. The difference arises from our insistence on designating the optical propagation axis as the z-axis. We shall also refer to this direction as the *axial* direction. For both types the *lateral* y-direction is in the plane of the substrate. For in-plane lasers the vertical to the substrate is the *transverse* x-direction, as illustrated in Fig. 1.7, whereas for vertical-cavity lasers the x-direction lies in the plane and is deemed a second lateral direction.

Once we have decided that a lateral patterning of the active region is desirable for lateral carrier and photon confinement, we also must consider lateral *current* confinement. That is, once the active region is limited in lateral extent, we must ensure that all the current is injected into it rather than finding some unproductive shunt path. In fact, current confinement is the first and simplest step in moving from a broad-area laser to an in-plane stripe or vertical-cavity dot laser. For example, current can be channeled to some degree simply by limiting the contact area. However, in the best lasers current confinement is combined with techniques to laterally confine the carriers and photons in a single structure.

Lateral confinement of *current*, *carriers*, and *photons* has been accomplished in literally dozens of ways, and there are even more acronyms to describe all of these. For brevity's sake, we will focus on only a few generic types illustrated in Fig. 1.17. Here we illustrate schematic transverse-lateral (x-y) edge-emitter laser

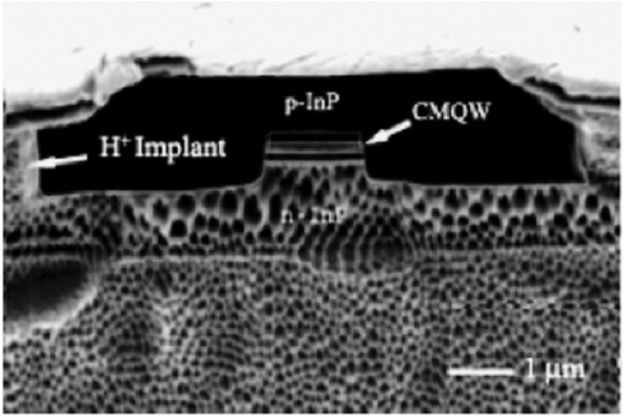

(*a*)

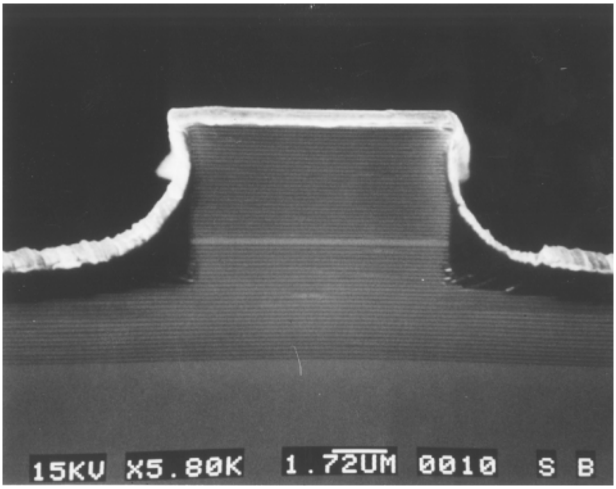

(*b*)

FIGURE 1.16: Cross-sectional SEMs of (a) in-plane and (b) vertical-cavity semiconductor lasers.

cross sections along with calculated optical mode intensity profiles. The first two types only provide current confinement, the third adds a weak photon confinement, and the last four provide all three types of confinement. The first four can be created by patterned etching, deposition, and implantation techniques typically found in semiconductor fabrication facilities, but the last three require at least one semiconductor regrowth step in addition, which is more specialized and perhaps costly. The examples are explicit for in-plane lasers, but many are also applicable to vertical-cavity lasers as illustrated by the analogous schematics shown in Fig. 1.18.

Figure 1.17a illustrates a simple oxide stripe laser. This stripe laser is the simplest to make because the area of current injection is limited simply by limiting

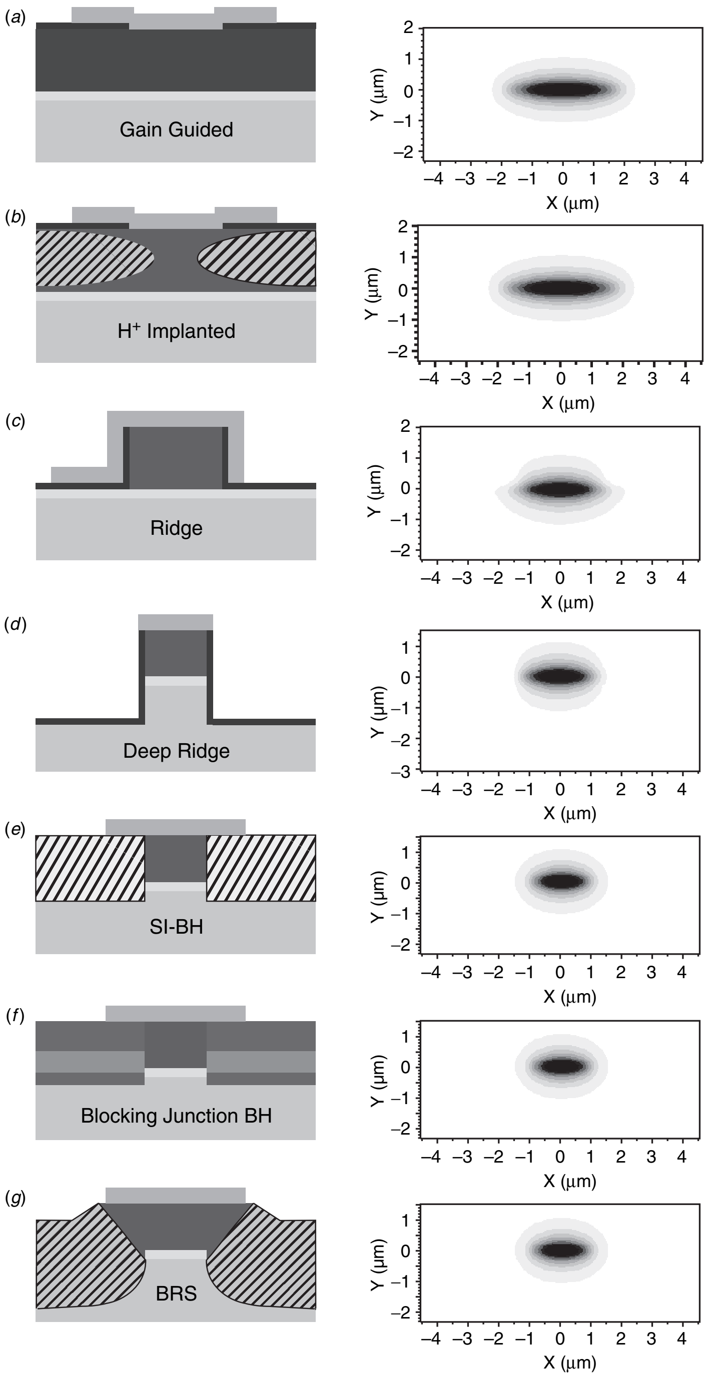

FIGURE 1.17: Lateral confinement structures for in-plane lasers: (a) oxide-stripe provides weak current confinement; (b) proton-implant provides improved current confinement; (c) ridge structure provides good current plus photon confinement; (d) deep-ridge gives strong current, carrier and photon confinement; (e) semi-insulating regrowth buried-heterostructure (SI-BH) provides good current, photon, and carrier confinement; (f) blocking-junction BH can provide current, photon, and carrier confinement; and (g) the buried-ridge-stripe BRS can also provide current, photon, and carrier confinement.

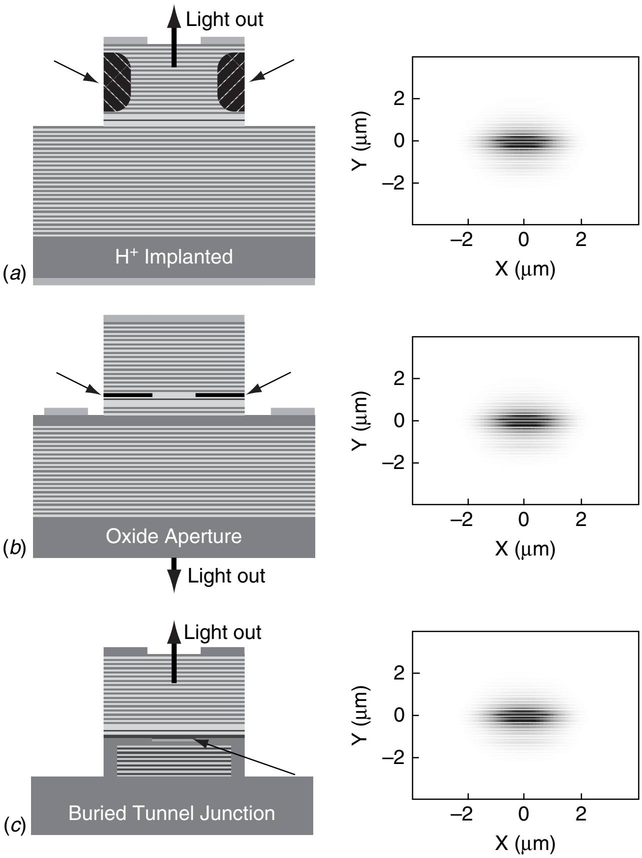

FIGURE 1.18: Schematics of VCSELs. (a) Proton-implanted, multimode with only current confinement; (b) dielectrically apertured with current and photon confinement; (c) mesa-confined with possible current and photon confinement.

the contact area. This laser has some current confinement, but no carrier or photon confinement. The proton-implanted configuration of Fig. 1.17b can provide current confinement by creating semi-insulating regions beneath the contact surface. It uses the fact that implanted hydrogen ions (protons) create damage and trap out the mobile charge, rendering the implanted material nearly insulating. Generally, the implant and resulting semi-insulating region is limited to a region between the contact and the active region, so that the contact can be wider while nonradiative recombination is avoided in the active region.

The configurations of Fig. 1.17a and b are described as *gain-guided* stripe lasers because the current is apertured, but there is no lateral index step or heterobarrier to provide a potential well for photons or carriers. Thus, carriers injected into the active region can diffuse laterally, decreasing the laser's efficiency, and there is also no lateral index change to guide photons along the axis of the cavity, so optical losses tend to be high. Although these two configurations were of some commercial importance in the early days of diode lasers before the advent of viable etching or regrowth techniques, currently their use is limited for commercial edge-emitters. However, multimode VCSELs, which use a relatively large diameter >10 microns, are still produced using the proton-implant technology because this can be done at very low cost. The oxide stripe laser is still used in the lab to characterize material because the processing is so simple, and proton isolation is still used to limit current leakage in combination with other confinement techniques in practical edge-emitters, but the implant areas are kept away from the active region for reduced loss and improved reliability.

Figure 1.17c illustrates a surface *ridge* laser that combines current confinement with a weak photon confinement. The efficiency of current injection can be high, but because the processing involves etching down to just above the active region, carriers are still not confined laterally. They are free to diffuse laterally and recombine without contributing to the gain. The etching depth is adjusted to provide just enough effective lateral index change to provide a single lateral mode optical waveguide. Quantum-well-SCH transverse waveguide structures together with selective chemical etches can provide the desired lateral index profiles and separation from the active region to avoid surface-related carrier recombination. The ridge structure continues to be a popular choice, both because of its fabrication simplicity and its reasonable performance characteristics, especially if operated far above threshold where the lateral carrier diffusion effects are less important because they saturate at threshold. Because of the weak optical confinement, the surface ridge only allows relatively large radius waveguide bends. For sharper bends a stronger lateral index step is needed. Figure 1.17d shows the case of a deeply etched ridge that provides strong lateral confinement of photons, carriers, and current. It provides for much sharper waveguide bends. However, in this case it is very important that the sidewalls be formed very smoothly to limit optical losses, and some procedure must be used to limit the nonradiative recombination of carriers at the surface of the active region, which forms an inherent array of defects. Also, the deeply etched ridge will need to be much narrow than the surface ridge to support only a single lateral optical mode. Thus, it may be more difficult to couple light into and out of it because of the resulting large diffraction angle, and its thermal impedance will also be higher because of its smaller connection area to the substrate.

Figures 1.17e, f, & g illustrate examples of *buried-heterostructure* (BH) lasers, in which the active region is surrounded by higher-bandgap, lower-index-of-refraction semiconductor materials so that carriers and photons are confined laterally as well as transversely. Thus, a lateral (y) cut through the active region gives very analogous plots for the bandgap and electric field as the transverse (x) cut in Fig. 1.7. The three different cases confine the injected current in three different ways to prevent it from leaking around the active region. The first (e) uses the growth of a semi-insulating layer of semiconductor on either side of an etched ridge to confine the current to flow only into the active region; the second (f) uses two or more reverse biased junctions in the regrown regions; and the third

(g) follows an overgrowth of doped material above and beside the active region by an implant to prevent current flow along the sides. In this latter case, the lower turn-on voltage of the active-region diode also tends to funnel the current through this region even without the lateral implants.

There are still other ways of forming BH lasers that are not illustrated in Fig. 1.17, using techniques such as *quantum-well intermixing* (QWI). For QWI, only one epitaxial growth is performed, and then the active layer to the left and right of the desired active stripe is *modified to increase its bandgap after growth* by the diffusion of impurities or vacancies across the quantum-well active region. The diffusing species cause an intermixing of the original cladding and active quantum-well lattice atoms by requiring them to hop from site to site as the diffusing species move through. Thus, the absorption edge energy of the quantum wells is increased in these regions providing lateral carrier confinement to the central undiffused region.

Figure 1.18 shows schematic VCSEL cross sections together with calculated optical mode profiles for three types of lateral confinement structures. These differ from Fig. 1.17 because for the VCSEL, axial-lateral (z-y) cross sections are given, even though cross sections of the epitaxial wafer with its surface normal being the vertical axis are shown in both cases. Circular symmetry in the x-y plane of the wafer is assumed. Nearly all VCSELs use quantum wells placed at a standing wave maximum of the electric field, as will be discussed in later chapters and specifically Appendix 5. The first case (a) illustrates a proton-implanted VCSEL that uses the implant to generate a current confinement aperture much like the edge-emitter of Fig. 1.17b. As already mentioned, these are usually formed with relatively large diameters >10 μm to deliberately have multimode outputs. The second example (b) illustrates the dielectrically apertured VCSEL. The aperture is usually formed by an oxidation of a AlAs or a high Al content AlGaAs layer very close to the active region (sometimes referred to as "oxide-confined"), although it has also been formed by an etched air-gap. The low-index, insulating aperture provides lateral current and optical confinement. As the aperture is close to the active region, the current confinement tends to be quite good. The optical confinement results from the lensing action of the dielectric aperture that refocuses light resonating between the two planar mirror stacks. Blunt apertures are generally used, and some optical scattering loss results, but if tapered to be more lenslike, these apertures can act as near perfect lenses and scattering losses or internal diffraction loss can be effectively eliminated [6]. The third VCSEL example (c) also provides good optical and current confinement, but in this case the inclusion of a small thickness semiconductor disk above the active region provides the optical lensing element. It also yields current confinement if the disk provides a lower resistance path to the active region than the surrounding areas. One popular approach is to form a low resistance tunnel junction layer structure that is etched off everywhere except for this small disk. This configuration does require a regrowth of the mirror material above the disk confinement element, whereas the first two VCSEL geometries can be formed after a single epitaxial growth step.

1.8 PRACTICAL LASER EXAMPLES

Figures 1.19 and 1.20 give cross-sectional schematics and illustrative characteristics of a number of experimental in-plane and vertical-cavity lasers. The figure captions contain some of the relevant descriptive details. In the chapters to follow, the operating principles of such lasers will be detailed.

Figure 1.19 illustrates results from five edge-emitting in-plane lasers. The first (a) is a simple gain-guided stripe laser that is illustrative of designs used for high-power pump lasers. In this case the active region is a strained InGaAs quantum well in an AlGaAs SCH waveguide to provide emission in the 910–990 nm range. Narrow stripe lasers that can be coupled into a single mode optical fiber and have wavelengths 980 nm of this general composition are used to pump Er-doped

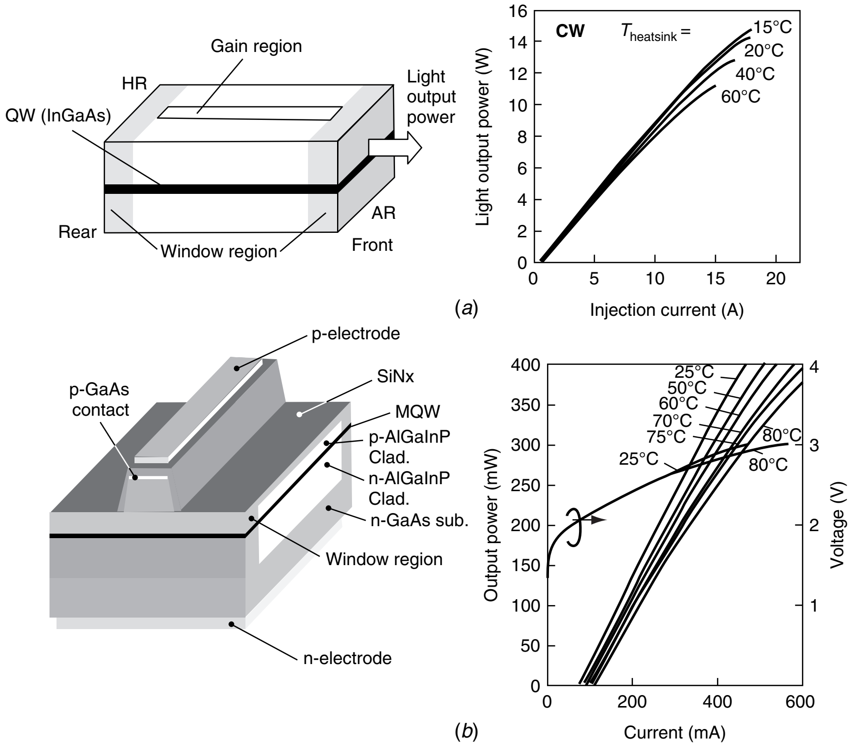

FIGURE 1.19: (a) schematic and *L-I* characteristic for 915 nm wavelength InGaAs/GaAs 100 μm wide broad-area laser using vacancy-induced QWI at the facets to avoid COD [7] (© IEEE 2007); (b) schematic and *L-I* characteristic for 650 nm wavelength AlGaInP/GaAs ridge laser using impurity-induced QWI at facets [8] (© IEEE 2007); (c) schematic and *L-I* characteristic of 404 nm wavelength InGaN/GaN ridge laser using nonpolar design [9] (© JJAP 2007); (d) schematic and *L-I* characteristic for 1300 nm wavelength InGaAlAs/InP MQW-DFB laser [10] (© IEEE 2006); (e) schematic and *L-I* characteristic of 1550 nm wavelength InGaAsP/InP SIBH-MQW-DFB laser [11] (© IEEE 2007).

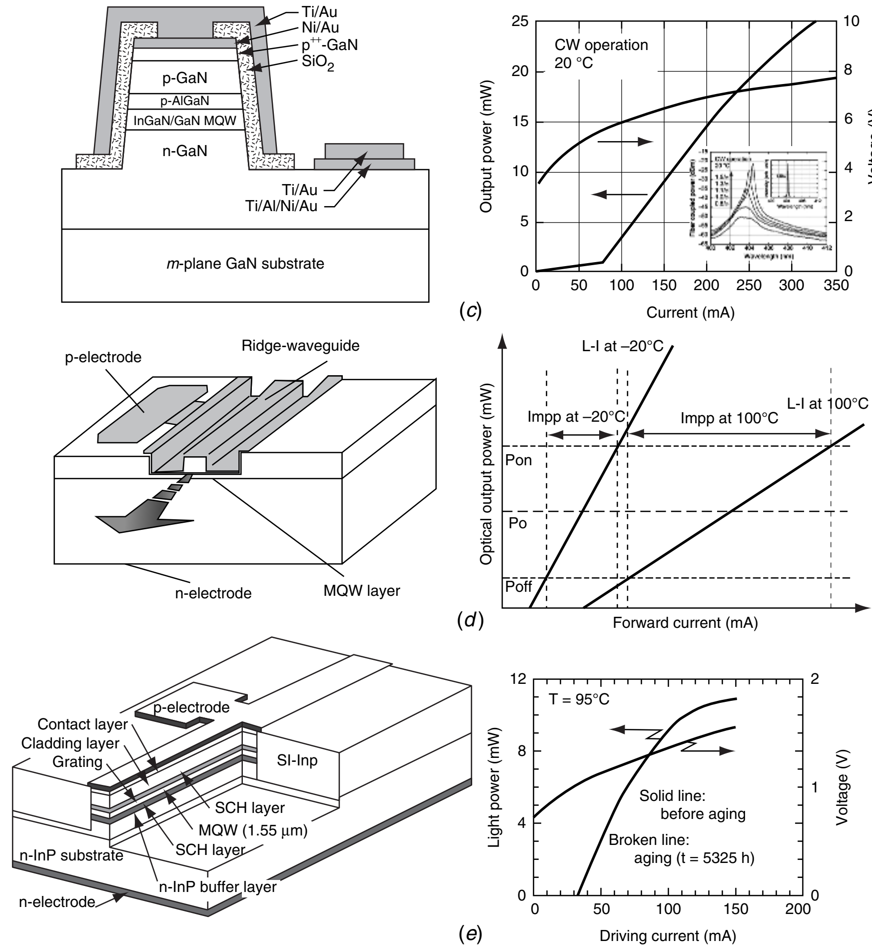

FIGURE 1.19: *(Continued)*

fiber amplifiers that are very important in optical fiber communication systems. Other important diode pumps include ones for pumping Nd-doped YAG, and these typically are composed of AlInGaP with emission in the 808 nm range. These are also formed on GaAs substrates.

An important limitation on the output power of such pump lasers is a catastrophic optical damage (COD) of the cleaved mirror facets due to nonradiative recombination of carriers at surface related defects and the resulting optical absorption and run-away heating. In the case of Fig. 1.19a, the COD is addressed by creating a nonabsorbing region near the facet by locally increasing the bandgap. The bandgap increase is accomplished by diffusing vacancies across the quantum well in this region to intermix the SCH and QW materials—what we have termed QWI above. The vacancy source results from the absorption of Ga ions by a special film deposited on the surface in this region. CW output powers of >8 W were obtained with input currents of 10 A up to temperatures of 60°C for 100-μm-wide stripes.

Other approaches have been employed to limit COD. QWI can also be achieved by diffusing impurities across the quantum-well active regions as well as vacancies. Some companies have also been able to develop surface passivation treatments and thin-film coatings that appear to limit COD and other forms of facet degradation during aging and high-power operation.

Figure 1.19b gives an example of a relatively high power AlInGaP/GaAs surface-ridge waveguide laser that emits at 650 nm. With the powers shown, it can be used for high speed DVD writing as well as reading. For this application the power out as well as the output beam shape need to be free from kinks and glitches over a wide range of input currents. Diffraction angles parallel and perpendicular to the substrate that differ at most by a factor of 2 are also desired. These are accomplished by using a relatively narrow ridge width that ensures a single lateral optical mode as well as a relatively circular output beam.

QWI was used to form a transparent window region near the facets to prevent COD in this device as well. In this case the QWI was accomplished by diffusing Zn from a thin film of ZnO deposited on the surface only within 10 μm of the cleaved facet. The facets were also coated with low reflectivity (3%) and high reflectivity (95%) coatings on the output and back facets, respectively.

Similar lasers, although with lower power requirements, are used in most DVD players. Similar designs are also used in a wide variety of other "red laser" applications that range from supermarket scanners, to handheld pointers, to indicator lines on carpenter's tools.

Figure 1.19c shows results from an experimental GaN-based ridge wave guide blue laser. In this case the device is a nonpolar InGaN/GaN design, which does not have an AlGaN cladding. Unlike most of the early GaN laser work that used c-plane (0001) structures, this one is grown on m-plane $(1\bar{1}00)$ that avoids polarization effects as well as increased problems with parasitic wave guides and threading dislocations. This device emits at 404 nm; it has a threshold current density of 6.8 kA/cm^2 and a threshold voltage of 5.6 V. Although significant improvements in output power and efficiency are expected with this design, it still will serve as a representative of an important class of lasers based on GaN and its related alloys: AlGaInN.

The AlGaInN system can provide direct bandgaps from the infared (InN) to the UV (AlN), but good lasers have only been made in the blue-green to the near UV range. Nevertheless, this is a very important range for a wide variety of applications. Blue and near UV diode lasers are of great interest for solid-state lighting, high density optical data storage, projection displays, optical sensing, and medical applications. "Blu-ray" Disc is an important commercial product at this writing, but projection displays and solid-state lighting may have the largest long-term impact.

Figures 1.19d and e illustrate fiber-optic communication sources, both based on the InP materials system. The first (d) is an InGaAlAs/InP multiple-quantum-well

(MQW) 1300-nm wavelength ridge-waveguide laser that uses a grating along its length to select a single longitudinal output mode. As discussed in Chapter 3, this distributed grating provides a distributed feedback or (DFB) mirror, so it is called a DFB laser. The 1300-nm wavelength is the point of lowest dispersion in optical fiber, and it is used to send high data rates over modest distances. Because it is not used in long-haul networks, this wavelength tends to be limited to metropolitan, local area, or on-campus networks.

As discussed previously, the InAlGaAs material system has most of the quantum-well bandgap offset in the conduction band, so it is better at confining the low-effective-mass electrons than the InGaAsP/InP system. In this example, this material is selected to enable the lasers to operate to higher temperatures so that thermoelectric coolers are not needed, and much lower cost, lower power packages can be made. By making the cavity short (200 μm) the relaxation resonance was also increased to >20 GHz even at 100°C. The laser is designed to operate with direct current modulation at a data rate of 10.7 Gb/s. The laser is never turned completely off, as indicted in Fig. 1.19d, but the on/off ratio is kept to ~7 dB.

Figure 1.19e illustrates a semi-insulating regrowth buried-heterostructure (SIBH) laser formed with multiple quantum wells in the InGaAsP/InP system for operation at 1550 nm, which is the wavelength of minimum loss in optical fiber. It also is a DFB laser to ensure single-mode operation. Long-haul communication systems desire single-mode sources at 1550 nm to maximize the distance possible between amplifiers or repeater nodes. Because it is not the natural dispersion minimum of optical fiber, this needs to be managed in some other manner. It is also the wavelength region used for wavelength division multiplexed (WDM) multichannel communication. Thus, 1550 nm also tends to be used in metro and local area networks as these extend toward the edge.

Figure 1.20a illustrates results from a proton-implanted, gain-guided vertical-cavity laser emitting at 850 nm. The active region uses GaAs quantum-wells, and the epitaxial mirrors are composed of alternate quarter-wave layers of AlGaAs having a low (~15%) and high (~85%) Al composition, respectively. About two dozen periods are needed to provide >99.5% reflectivity as required to reach threshold in practical environments given the very small gain length (typically, the thickness of three quantum wells ~8 nm each) in these devices. The proton implant is generally concentrated midway between the top contact and the active region within the top, p-type mirror stack. It is usually slightly larger in diameter than the emission window in the top contact. This positioning ensures a low overall resistance path from the contact as well as a good aperturing of the current without damaging the carrier lifetime in the active region. This latter point emphasizes that a proton implant is *not* a carrier confinement approach, but rather just the opposite—it yields near zero carrier lifetime, so allowing the proton implant to extend into the lateral extremes of the active region would drain away carriers faster than simply allowing them to laterally diffuse away.

The GaAs-based device of Fig. 1.20a was the earliest type of VCSEL to be qualified for use in telecommunication systems and widely used with multimode fiber in data communication (datacom) links. As multimode fiber has core diameters

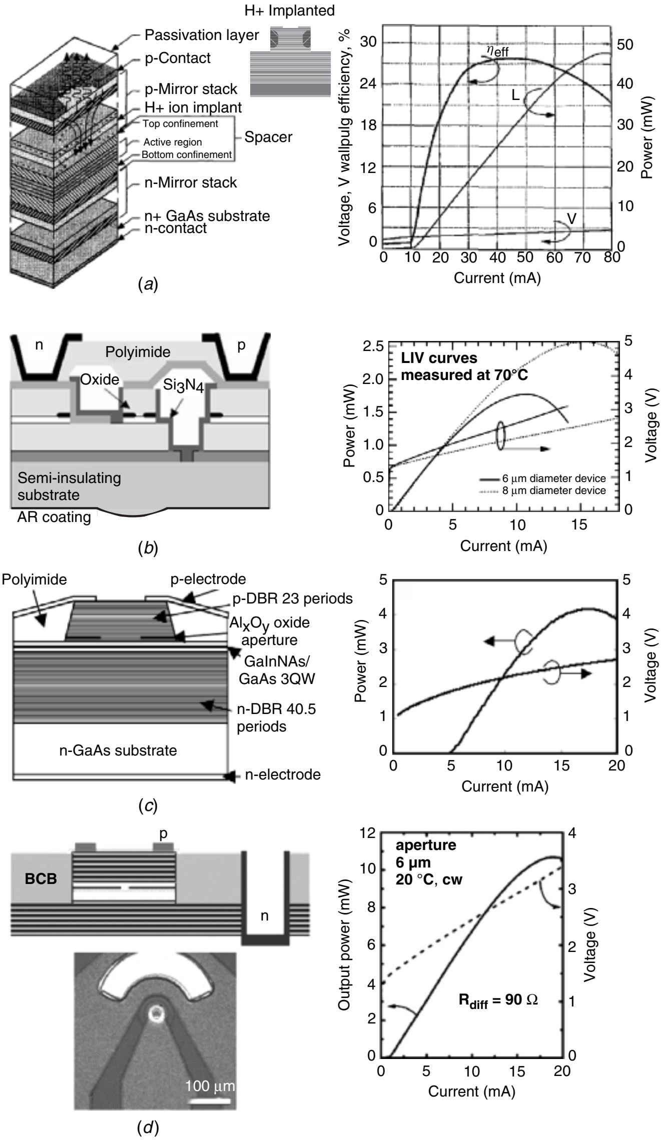

FIGURE 1.20: Practical VCSEL examples: (a) schematic and *L-I* characteristic for proton-implanted 850 nm wavelength AlGaAs/GaAs laser with 15 μm contact window and 20 μm diameter implant [12] (© IEE 1995); (b) schematic, *L-I* and temperature characteristics of 985 nm InGaAs/GaAs oxide-apertured VCSEL with an integrated backside microlens [13] (© IEEE 2007); (c) schematic and *L-I* characteristic of GaInNAs/GaAs VCSEL emitting at 1262 nm [14] (© IEEE 2007); (d) schematic, *L-I,* and temperature characteristics of 980 nm InGaAs/GaAs quantum-dot VCSEL [15] (© IEEE 2007); (e) schematic and L-I characteristics for both 1300 and 1550 nm InGaAlAs/InP VCSELs incorporating one dielectric mirror and a tunnel junction confinement structure [19] (© IEEE 2005).

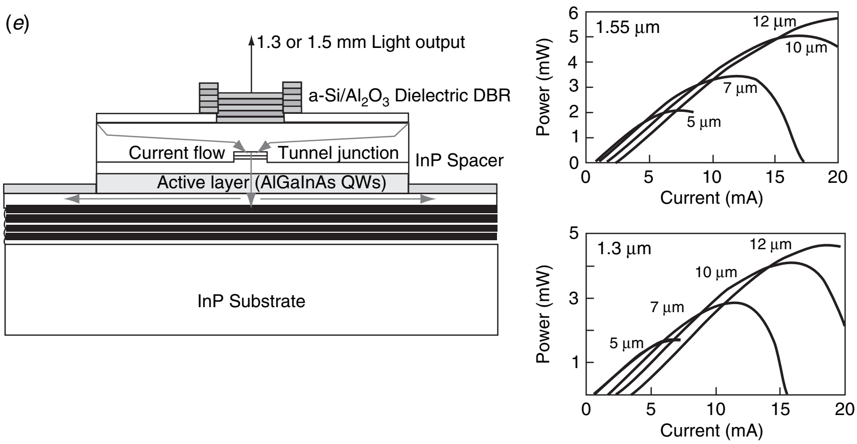

FIGURE 1.20: *(Continued)*

~50–60 μm, VCSEL diameters of ~20 μm with many lateral lasing modes are typically used. “Gigabit Ethernet” and “Fiber-channel” are examples of IEEE link standards that incorporate such VCSEL sources. Data rates in the gigabit per second range and distances up to a few hundred meters are typically involved. Linear arrays of such VCSELs together with fiber ribbon cable have also found applications in parallel data links, which can multiply the overall link capacity by 10 or more times.

A key attribute of the datacom links incorporating such multimode VCSELs and fiber is their low cost, given the relatively high level of performance. Unlike edge-emitters, VCSELs can be manufactured and tested at wafer scale—no cleaves or edges are necessary to evaluate them. Because of the large multimode fiber core and the small, circular diffraction angle of the VCSEL emission, passive alignment techniques are possible in the packaging of the VCSEL. Optical connectors can also be simple. All of this enables low cost production.

Figure 1.20b shows a somewhat more complex VCSEL design that employs an oxide aperture for lateral current and photon confinement. Illustrated is a bottom-emitting device with an InGaAs MQW active region emitting at 980 nm, GaAs/AlGaAs mirror stacks, and an integrated microlens. As shown, trenches must be etched down to the AlAs oxidation layer just above the active to perform the lateral oxidation after the epitaxial growth of the semiconductor layers. As illustrated, oxide-apertured devices can easily be formed with smaller diameters that support single-mode operation and very low threshold currents. The use of the InGaAs strained quantum wells provides an emission at which the GaAs substrate is transparent, and this enables bottom emission and flip-chip bonding for good heat sinking and simple packaging, including the option of integrated, prealigned microlenses on the backside of the substrate. The InGaAs also has better gain properties for more efficient and higher modulation bandwidth operation. However, for many datacom applications the standards have been adopted for 850 nm, so many of these advantages go unrealized in systems.

The temperature characteristics shown in Fig. 1.20b also show another interesting feature designed into most modern VCSELs. Because the cavity is so short and the multilayer mirror reflectivity band is narrow, only a single axial mode can lase, and this tunes with temperature at the rate of $\sim$0.1 nm/$^\circ$C due to the change in the index of refraction. Also, the gain has a maximum value near the energy separation between the lowest quantum-well levels in the conduction and valence bands, but this tunes in temperature at the rate of $\sim$0.5 nm/$^\circ$C due to the change in bandgap energy. Thus, there is a differential tuning of the gain and mode wavelength, or explicitly, the peak gain will tune across and past the mode wavelength at a rate of $\sim$0.4 nm/$^\circ$C. So the trick is to deliberately misalign the peak gain at room temperature and as the temperature rises, enable the gain to move into alignment with and then past the mode. Of course, this results in a wide region of relative insensitivity to temperature.

Figure 1.20c illustrates another oxide-confined GaAs-based VCSEL, but in this case the MQW-active region is composed of GaInNAs, or a similar composition to Fig. 1.20b with a few percent of nitrogen added. Somewhat counterintuitively, the result is a significant increase in the emission wavelength toward 1300–1262 nm in this case. Normally, one might expect that the addition of a smaller atom to an alloy would reduce the wavelength, as in the case of GaN, for example. The difference here is that the N is so different in atomic size that it doesn't fit into the GaAs lattice in a normal bonding configuration. So, in small percentages, it creates a local deviation in the lattice potential, much like an impurity or a defect might, but of course it has the right valence, so it is neither. But, it does have the effect of pulling the conduction band down a bit resulting in the lower transition energy. Another complementary effect is that the smaller size of the N adds tensile strain, partially compensating the compressive strain of the In, and thus enabling an increase in the In composition, and this also tends to increase the emission wavelength.

The key reason for pursuing efforts with this material has been the ability to make GaAs-based VCSELs with well-developed high index contrast AlGaAs/GaAs mirror stacks and AlO_x oxide confinement, but with wavelengths $\sim$1300 nm for longer-reach datacom applications. However, there have also been problems associated with reproducibility of the wavelength and gain properties of the GaInNAs quantum wells. A critical annealing step generally has been found to be necessary to bring out the optimal properties of the material, and transfer to a manufacturing environment has not always been successful. Although good insensitivity to temperature variations has been reported, this appears to be due to a large nonradiative component that is temperature insensitive. Thus, the efficiency has generally not been comparable to other GaAs-based VCSELs, or even as good as the best InP-based long wavelength VCSELs as discussed later. Nevertheless, the GaInNAs approach may still be the most cost effective if high performance is not needed.

Figure 1.20d gives an example of a GaAs-based VCSEL with a quantum-dot active region. Although many efforts with quantum-dot actives on GaAs have aimed to push the wavelength out to the 1300-nm range using increased strain InAs dots, this example emits at 980 nm. It uses a growth procedure that avoids a lateral interconnecting "wetting layer" common to most other quantum dot devices that have shown relatively slow modulation responses. Tilted indium-rich columns result from a multisubmonolayer growth procedure. In this case direct modulation to 20 Gb/s at 85°C was demonstrated for the 6-μm diameter device characterized in the figure. In this case, over 10 mW of power is emitted at room temperature, and the threshold current is again engineered to decrease with temperature due to a deliberate gain-mode peak offset as discussed earlier.

Figure 1.20e introduces an InP-based VCSEL technology that incorporates an etched-tunnel-junction mesa as the current and photon confinement element. Results for both 1300- and 1550-nm emission are shown. InP-based VCSELs generally suffer from at least three problems relative to their GaAs-based counterparts. First, there are no well-developed lattice-matched mirrors that have high index contrast and high thermal conductivity; second, there is no simple well-developed oxide aperturing technology; third, the active materials tend to have somewhat lower gain per unit current and to be more sensitive to temperature. The configuration of Fig. 1.16e addresses most of these issues. However, a number of other alternative fabrication technologies have also been explored over the years. These include (1) wafer bonding GaAs-based mirrors onto an InP-base active region [16]; (2) use of a very thick InGaAsP bottom (output) mirror stack together with a lattice mismatched (metamorphic) GaAs/AlAs mirror stack for a top mirror [17]; and (3) use of lattice-matched high-index contrast GaAlAsSb mirror stacks in an all-epitaxial InP-based structure [18]. After some development, none have been manufactured in any volume. Of course, long-wavelength GaAs-based VCSELs have also been researched using both GaInNAs and quantum-dots, as already mentioned.

In the case of Fig. 1.20e, three key layer structures are grown in sequence. First the bottom semiconductor mirror stack, bottom n-type contact layer, active region, a thin p-type layer, and the $p^+ - n^+$ tunnel junction are formed on the InP substrate. The tunnel junction, which enables low-resistance n-type contacts to the top as well as the bottom of the diode, is then etched away except where the optical mode is to exist. In the second semiconductor growth, the n-type InP spacer/top contact layer is grown over the tunnel junction mesa and the rest of the p-type top surface. Note that no current will flow across the reverse biased n–p junction except where the tunnel junction exists. Ohmic contacts are formed to the InP spacer. Finally, the top amorphous-Si/Al_2O_3 dielectric mirror stack is grown. Because the tunnel junction also adds optical length to the center of the cavity, it also acts as a lensing element to confine to optical mode to this region. The thermal impedance can be kept relatively low in this design if heat sinking is added to the top InP layer because it has relatively good thermal conductivity. This can be addressed by designing the device for bottom emission and flip-chipping it onto a heat sink. There has been similar work that has emphasized this approach [20].

The applications for these long wavelength VCSELs are in single-mode fiber data links with data rates ~10 Gb/s (e.g., 10 Gigabit Ethernet or 10 GbE) and distances extending to tens of kilometers. Parallel data links for applications like

100 GbE are also being developed. Competition with simple edge-emitting solutions such at those in Fig. 1.19d and 1.19e are key issues. The low-cost manufacturability of VCSELs remains one of the possible advantages, but as the VCSELs become a little more complex this becomes a weaker argument.

REFERENCES

1. Hirtz JP, Razeghi M, Bonnet M, Duchemin JP. Ga.sub.0.47 In.sub.0.53 As/InP double heterostructures grown by low-pressure metal-organic vapour-phase epitaxy. In: Pearsall TP, editor. *GaInAsP alloy semiconductors*. New York: Wiley; 1982. P 61–83.
2. Vurgaftman I, Meyer JR, Ram-Mohan LR. Band parameters for III–V compound semiconductors and their alloys. *J Appl Phys* 2001;**89**:5815.
3. Hayachi I, Panish MB, Foy PW, and Sumski S. *Appl. Phys. Lett.*, 1970;**109**:17.
4. Chaub KY, and Cho AY. *J. Appl. Phys.*, 1982;**53**:441.
5. Vurgaftman I, Meyer Jr. Band parameters for nitrogen-containing semiconductors. *J Appl Phys* 2003;**94**:3675.
6. Coldren LA, Thibeault BJ, Hegblom ER, Thompson GB, Scott JW. Dielectric apertures as intracavity lenses in vertical-cavity lasers. *Appl Phys Lett* 1996;**68**:313.
7. Taniguchi H, Ishii H, Minato R, Ohki Y, Namegaya T, Kasukawa A. 25-W 915-nm lasers with window structure fabricated by impurity-free vacancy disordering (IFVD). *IEEE Journal of Selected Topics in Quantum Electronics*. 2007;**13**(5):1176–1179.
8. Sumitomo H, Kajiyama S, Oguri J, Sakashita T, Yamamoto T, Nakao K, Domoto S, Ueda M, Amano H, Satoyoshi H, Kita T, Izumi, S. Uniform and high-power characteristics of AlGaInP-based laser diodes with 4-inch-wafer process technology. *IEEE Journal of Selected Topics in Quantum Electronics* 2007;**13**(5):1170–1175.
9. Farrell RM, Feezell DF, Schmidt MC, Haeger DA, Kelchner KM, Iso K, Yamada H, Saito M, Fujito K, Cohen DA, Spec JS, DenBaars SP, Nakamura S. Continuous-wave operation of AlGaN-cladding-free nonpolar *m*-plane InGaN/GaN laser diodes. *Jpn J Appl Phys* 2007;**46**:L761–L763.
10. Singh H, Motoda K, Mukaikubo M, Okamoto K, Washino R, Sakuma Y, Uchida K, Yamamoto H, Uomi K, Nakahara K, Aoki M. Proceedings of Optical Fiber Communication Conference and National Fiber Optic Engineers Conference; 2006 Mar 5–10.
11. Takeshita T, Tadokoro T, Iga R, Tohmori Y, Yamamoto M, Sugo M. Highly reliable 1.5-μm DFB laser with high-mesa SIBH structure. *IEEE Transactions on Electron Devices* 2007;**54**(3):456–461.
12. Morgan FA, Hibbs-Brenner MK, Walterson RA, Lehman JA, Marta TM, Bounnak S, Kelweit EL, Akinwande R, Nohava JC. Producible GaAs-based MOVPE-grown vertical-cavity top-surface emitting lasers with record performance. *Electronics Letters* 1995;**31**:462.
13. Lin C-K, Tandon A, Djordjev K, Corzine SW, Tan MRT. High-speed 985 nm bottom-emitting VCSEL arrays for chip-to-chip parallel optical intercommects. *IEEE Journal of Selected Topics in Quantum Electronics* 2007;**13**(5):1332–1339.
14. Nishida T, Takaya M, Kakinuma S, Kaneko T. *IEEE Journal of Selected Topics in Quantum Electronics* 2005;**11**(5):958–961.
15. Hopfer F, Mutig A, Fiol G, Kuntz M, Shchukin BA, Haisler FA, Warming T, Stock E, Mikhrin SS, Krestnikov IL. 20 Gb/s 85°C error-free operation of VCSELs based on

submonolayer deposition of quantum dots. *IEEE Journal of Selected Topics in Quantum Electronics* 2007;**13**(5):1302–1308.

16. Okuno YL, Gan K-G, Chou J-F, Chiu Y-J, Wang CS, Wu S, Geske J, Bjorlin ES, Bowers JE. *IEEE Journal of Selected Topics in Quantum Electronics* 2005;**11**(5): 1006–1014.
17. Starck C, Plais A, Derouin E, Pinquier A, Gaborit F, Fortin C, Goldstein L, Boucart J, Salet P, Carpentier D. Indium phosphide and related materials. 1998 International Conference on. 1998 May 11–15. P369–372.
18. Nakagawa S, Hall, E, Almuneau G, Kim JK, Buell DA, Kroemer H, Coldren LA. 1.55-μm InP-lattice-matched VCSELs with AlGaAsSb-AlAsSb DBRs. *IEEE Journal of Selected Topics in Quantum Electronics* 2001;**7**(2):224–230.
19. Nishiyama N, Caneau C, Hall B, Guryanov G, Hu MH, Liu XS, Li M-J, Bhat R, Zah CE. Long-wavelength vertical-cavity surface-emitting lasers on InP with lattice matched AlGaInAs– InP DBR grown by MOCVD. *IEEE Journal of Selected Topics in Quantum Electronics* 2005;**11**(5):990–998.
20. Amann M-C, Hofmann W. InP-based long-wavelength VCSELs and VCSEL arrays. *IEEE Journal of Selected Topics in Quantum Electronics* 2009;**15**(3):861–868.

READING LIST

P. Bhattacharya, *Semiconductor Optoelectronic Devices*,Chs. 1 and 2, Prentice Hall, Englwood Cliffs, NJ (1994).

B.E.A. Saleh and M.C. Teich, *Fundamentals of Photonics*, Chs. 15 and 16, Wiley, New York (1991).

A. Yariv, *Optical Electronics*, 4th ed., Ch. 15, Saunders College Publishing, Philadelphia (1991).

G. P. Agrawal and N. K. Dutta, *Semiconductor Lasers*, 2d ed., Chs. 4 and 5, Van Nostrand Reinhold, New York (1993).

PROBLEMS

These problems draw on material from Appendices 1 through 3.

1. Define the necessary elements of a laser cavity.
2. A laser cavity is formed by two ideal mirrors with flat frequency response over the 1.4–1.6 μm wavelength range, positioned 1 mm apart, by an ideal bandpass filter centered at 1.55 μm and 4 nm wide, and by a gain region with a parabolic function gain function $g = -7.5 \cdot 10^{12}\ \mathrm{cm}^{-3}(\lambda - 1.55\ \mu\mathrm{m})^2 + 10^4\ \mathrm{cm}^{-1}$. For this simple cavity, referring to Fig. 1.1, determine the lasing wavelength of this laser. Assume that most of the photons are propagating through free space.
3. List three advantages and three disadvantages diode lasers have relative to gas or solid-state lasers.

4. What are the most common applications of diode lasers? Can you think of any other applications not mentioned in the text?

5. What is the difference between the energy levels in the solid state and diode lasers?

6. List and explain all the basic electronic recombination/generation mechanisms. Which one is required for lasers to operate?

7. Describe the main ways of nonradiative recommbination in semiconductor lasers.

8. Explain how a double heterostructure works. Who are the Nobel prize winners for this invention?

9. Discuss the differences in carrier transport and recombination in direct-bandgap double heterostructure PN junctions relative to indirect-bandgap homojunction PN junctions?

10. A blue diode laser cross section consists of a set of five 80-nm-wide InGaN quantum wells with 12% In and 88% Ga, surrounded by six 80-nm-wide GaN barriers, and clad by P and N type GaN.

(a) Determine the effective index of the fundamental transverse mode of this waveguide. To do this, simplify the structure by calculating an average optical index of refraction for the quantum well/barrier region.

(b) Determine the rate of decay of the normalized transverse electric field U.

11. Give three differences between using a bulk active region and a quantum-well active region in a diode laser.

12. What are the fundamental requirements for the different materials involved in forming a complex separate-confinement heterostructure?

13. Why are III-V materials better than Si for LEDs and lasers?

14. What type of lasers is the GaAs/AlGaAs material system used for? How about InP/InGaAsP?

15. What is band offset, and why is it important? How much of the band offset occurs in the conduction band for (1) GaAs based lasers (2) InP based lasers?

16. An electron is trapped in a one-dimensional potential well 5 nm wide and 100 meV deep.

(a) How many bound energy states exist?

(b) What are the energy levels of the first three measured relative to the well bottom?

(c) If the well energy depth were doubled, how many states would be confined? (Assume the free electron mass.)

17. Repeat Problem 16 for a 10-nm-wide GaAs well and AlGaAs barriers.

18. Ten potential wells that each have two bound states are brought together so that their wavefunctions overlap slightly. How many bound energy states exist in this system?

19. How can the temperature range of InGaAsP lasers be extended?

20. The Blu-ray DVD disc has a much higher capacity than the original DVD disc. Explain how this was accomplished. How would you create an even higher capacity optical disc?

21. List two major manufacturers of the MOCVD growth systems.

22. Redo Example 1.2 for an InP-based VCSEL using AlInGaAs/AlInAs DBR mirror stacks. That is, determine the percentage of Al and In in the AlInAs layers to lattice match to InP.

23. Plot the minimum bandgap versus lattice constant for InAlSb. The bowing parameters for the direct, and the first indirect valley are 0.43 eV and 0 respectively. At which composition and lattice constant does the indirect bandgap equal direct bandgap?

24. A very long one-dimensional chain consists of atoms covalently bonded together with a resulting center-to-center spacing of 0.3 nm. The band structure of this system can be determined from the overlap of the individual atomic wavefunctions. The coupling energy given by Eq. (A1.21) for a particular atomic energy level, E_a, is 0.2 eV.

(a) Calculate the band structure over the first two Brillouin zones.

(b) Calculate the electron effective mass at the band extrema.

25. A light source emits a uniform intensity in the wavelength range $0.4 - 2.0$ μm. A polished wafer of GaAs with antireflection coatings on both surfaces is placed between the source and an optical spectrum analyzer.

(a) Sketch the wavelength spectrum received.

(b) Which processes in Fig. 1.6 are significant in forming this spectrum?

26. The light source in Problem 1.25 is replaced by a GaAs laser emitting at 850 nm, and it is found that 99.5% of the incident light is absorbed in the GaAs wafer. Now an Ar-ion laser emitting at 488 nm is trained to the same place on the wafer.

(a) As the power of the Ar-ion laser is increased to 3 W, the absorption of the GaAs laser beam is reduced to 50%. Assuming the heat is conducted away, explain what might be happening.

(b) The power in the Ar-ion laser is further increased, and it is found that at about 10 W the GaAs laser beam passes through the wafer unattenuated. Again, neglecting heating effects, explain why it requires 10 W rather than ~6 W to reach transparency.

27. For good carrier confinement it has been found that the quasi-Fermi levels should remain at least 5 kT below the top of a quantum well at operating temperature. In a particular GaAs quantum-well SCH laser, the operating active region temperature is found to be 125°C. If the quantum well is 80 Å wide, how much Al should be in the separate confinement region to provide the desired 5 kT margin in the conduction band at a carrier density of 4×10^{18} cm^{-3}?

28. (a) Plot the carrier density vs. the quasi-Fermi level for the conduction band in bulk GaAs and InGaAsP (1.3 μm) at 300 K. Cover the carrier density range from 1×10^{17} cm^{-3} to 1×10^{19} cm^{-3}, and use a logarithmic scale for the carrier density axis.

(b) With this result answer Problem 9 for a AlGaAs/GaAs bulk DH structure.

29. Calculate the density of states vs. energy for a "quantum wire" potential well in which two dimensions are relatively small. That is, assume a large dimension ($\gg$10 nm) in the z-direction and quasi-continuous state energies only for k_z.

30. Calculate the density of states vs. momentum for a quantum well.

31. Derive Eq. (A3.3).

32. Photons are transversely confined in a simple three-layer waveguide in a DH laser consisting of an InGaAsP active region 0.2 μm thick sandwiched between InP cladding layers. The bandgap wavelength of the active region is 1.3 μm.

(a) How many transverse TE modes can exist in this slab waveguide?

(b) Plot the transverse electric field for the lowest-order TE mode.

(c) What is the energy density 0.5 μm above the active-cladding interface relative to the peak value in the active region?

(d) What is the effective index of the guided mode?

(e) What is the transverse confinement factor?

33. Suppose the DH laser of Problem 1.32 is now used to form a BH laser with an active region 2 μm wide and InP lateral cladding regions, as in Fig. 1.17.

(a) What is the effective index for the fundamental two-dimensionally guided mode?

(b) How many lateral modes are possible?

(c) What is the lateral confinement factor for the fundamental mode?

34. VCSELs have been formed by etching 5 μm square pillars through the entire laser structure, creating rather large index discontinuities at the lateral surfaces. Assuming the axial propagation constant, β, is fixed at the same value for all resonant modes, and that the lowest-order mode has a wavelength of 1.0 μm, plot the mode spectrum including the first six lateral modes.

35. Derive Eq. (A3.14) and verify Eq. (A3.15).

36. It has been proposed that if the lateral dimensions of VCSELs or in-plane lasers become sufficiently small, the density of states for electrons and holes can be modified by the lateral size effect. In VCSEL material with an 80 Å thick GaAs quantum-well active region and high barriers, devices of various lateral widths are formed. How narrow must the device be before the lateral size effect shifts the lowest state energy up by 10 meV (about $\frac{1}{2}$ kT at room temperature)? Neglect any indirect surface-state pinning effect.